CHAPTER

10 Mechanics of Natural Fractures and Faults

In this chapter we use the knowledge of stress and mechanics of brittle fracture that is presented in the preceding two chapters to gain a deeper understanding of brittle deformation. With that background we can reexamine fractures and faults described in Chapters 3 through 7 and draw some conclusions about the conditions under which they form.

It is worth mentioning at the outset that in cases of complex deformation history, structures may be difficult to interpret, either because the relative timing of the formation of different structures is obscure or because structures form under one set of conditions and are reactivated under another. Thus, for example, it may be difficult to determine whether a set of fractures were formed before or during folding; fractures may develop as extension fractures and subsequently be reactivated with shearing displacement along them; and faults initiated with thrust displacement may be reactivated as normal faults. Such complexities make the interpretation of structures challenging and sometimes controversial.

With that caution in mind, then, we examine first the magnitude and origin of stress within the Earth, next the formation of extension fractures, and finally the formation of faults.

10.1 Techniques for Determining Stress in the Earth

Techniques for determining the state of stress in the Earth were developed largely in the geological engineering, mining, and energy industries. In mining, knowledge of the state of stress is important for the design of safe tunnels and stable open pits. In dam construction, the stresses in the abutments are measured before, during, and after construction to ensure safe design and operation. In oil and geothermal energy production, artificially fracturing rocks at depth can increase their permeability, thereby enhancing the yield from wells. Control of artificial fracturing requires knowledge of the state of stress at depth.

We also need to know the state of stress within the Earth in order to understand how and why plates move; why, where, and when earthquakes occur; and why and how structures form. Because of these practical and fundamental needs, the determination of stress in the Earth has become a field of geologic investigation in its own right.

Techniques are available for determining the current state of stress in the Earth as well as for determining

the "paleostress" that existed at some time in the geologic past. Some techniques provide a complete determination of the orientation and magnitude of the principal stresses; others provide only a partial determination of the state of stress. We discuss here techniques that rely on the effects of elastic or brittle deformation; those that rely on the effects of ductile deformation we discuss in Chapter 19 (see Box 19.2).

Stress Relief Measurements

Stress relief techniques of determining stress depend on the fact that the stress on an elastic material produces a proportional strain (see Section 9.1). When the stress is removed, the strain disappears, and measurement of the change in strain that accompanies unloading can be used to infer the original stresses, provided that the elastic constants of the rock are known independently.

Overcoring is a common technique that involves drilling a hole in the rock, attaching strain gauges to the surface of the hole, and then drilling an annulus around the hole to form a hollow cylinder of rock on which the stress from the surrounding rock has been released (Figure 10.1*A*). The release of stress causes elastic deformation of the cylinder, so its dimensions and its initial circular cross section change. Using the theory of elastic deformation (see Equation 9.5, for example), we can calculate the magnitude and direction of the original stresses from measurements of this deformation. The calculation is not simple, however, because the presence of the first hole changes the stress from its value in the solid rock, and this effect must be accounted for. For technical reasons, the maximum practical depth of boreholes for overcoring is 30 m to 50 m.

The flat jack is an instrument used to measure the normal component of stress acting on a plane of a particular orientation. Reference pins are inserted into the rock to form a rectangular grid, and the distances d_i $(i = 1, \ldots, 6)$ between pins are measured (Figure 10.1*B*). A slot is then cut into the rock which relieves the stress locally and changes the distances between the reference pins. A thin, hollow steel plate, the flat jack, is inserted into the slot, and the slot is filled with grout. When the grout has hardened, oil pressure in the hollow flat jack is increased until the reference pins return as closely as possible to their original relative positions. The measured oil pressure is then the normal component of stress acting in the rock across the plane of the flat jack. Several such measurements in different orientations can be used to determine the complete state of stress in the rock. This technique is commonly used in tunnels.

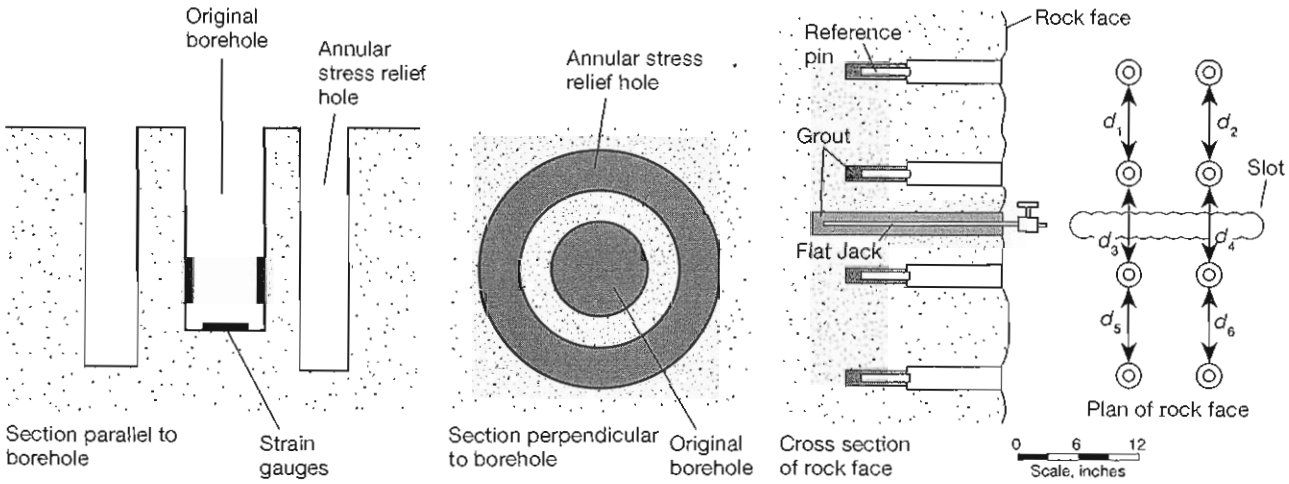

Figure 10.1 Stress relief techniques for measuring stress. *A*. Stress relief by the overcoring technique. A shallow borehole not exceeding 50 m in depth is drilled, and strain gauges are glued to the surfaces of the hole. An annular hole concentric with the first hole releases the stresses on the hollow cylinder of rock, and the resulting strain is measured by the strain gauges. Strain is converted to stress by means of the equations of elasticity and the elastic constants for the rock. *B*. The flat jack technique measures the component of stress normal to a plane of a particular orientation in the rock. An array of reference pins is inserted into the rock face, and the distances $d_1, d_2, \ldots, d_6$ between them are measured. A slot is cut, releasing the stress across the face of the slot. The flat jack is grouted into place in the slot. Pressurizing the flat jack with hydraulic fluid returns the reference pins to their original relative distances when the fluid pressure equals the original normal stress across the plane of the flat jack.

Hydraulic Fracturing (Hydrofrac) Measurements

Hydraulic fracturing, commonly abbreviated "hydrofrac," is a technique for fracturing the rock that, with some simplifying assumptions, makes it possible to determine both the magnitudes and orientations of the principal stresses. The techniqne was initially developed to increase the permeability of oil-bearing rocks penetrated by wells.

A section of a borehole is sealed off with two inflatable rubber packets (Figure 10.2*A*), and the fluid pressure between the pressure seals is pumped up until, at a critical pressure P_c, a tension fracture forms at the borehole. The fluid is sealed in immediately after fracturing occurs, and the pressure drops and stabilizes at a valne called the instantaneous shut-in pressure P_s, which is the pressure that is just sufficient to keep the fracture open.

Because the surface of the Earth is a free surface on which rhe shear stress must be zero, the principal stresses there must be perpendicular and parallel to the surface, or approximately vertical and horizontal. We assume the stresses at depth have the same orientation. If we assume that the borehole is vertical and that the tension fracture is parallel to it, the instantaneous shut-in pressure equals the minimum horizontal compressive stress in the rock; that is, $P_s = \sigma_{H(\min)}$. The critical pressure P_c is the sum of the minimum compressive sttess tangent to the surface of the botehole and the tensile strength T_0 of the rock. The elastic theory of a hole in a stressed solid shows that P_c depends on T_0, $\sigma_{H(\min)}$, and $\sigma_{H(\max)}$. Knowing P_c, T_0, and $\sigma_{H(\min)}$, we can calculate $\sigma_{H(\max)}$ from that relationship. The vertical normal stress is assumed to be equal to P_c and to the stress caused by the weight of the overlying rock, the overburden stress $P_c = \sigma_V = \rho_r g h$. $\sigma_{H(\min)}$ is perpendicular to the fracture, whose orientation is determined by using a downhole releviewer or by making an oriented impression of the surface of rhe borehold (Figute 10.2*B*). Thus all three principal stresses and their orientations are determined. Measurements at depths of up to 5 km have been achieved.

Stress Orientations from Earthquake First-Motion Studies

Earthquakes result from tegional stresses in the Earth, and they occur at depths ranging from shallow up to

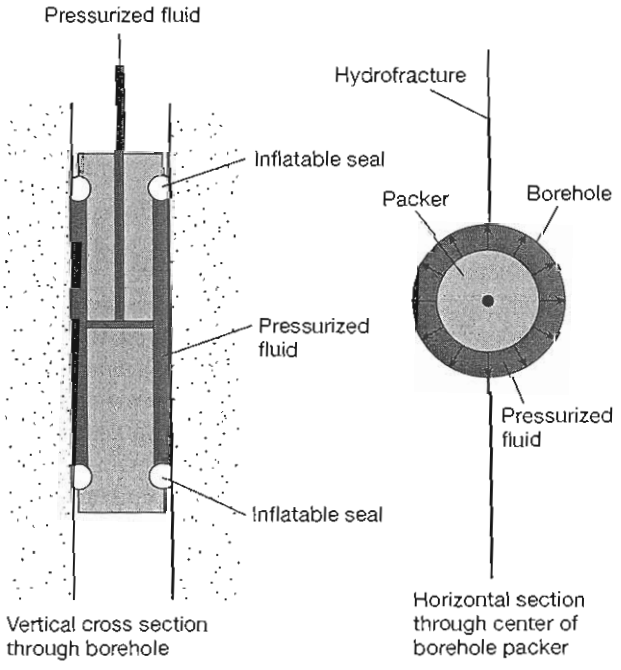

A.

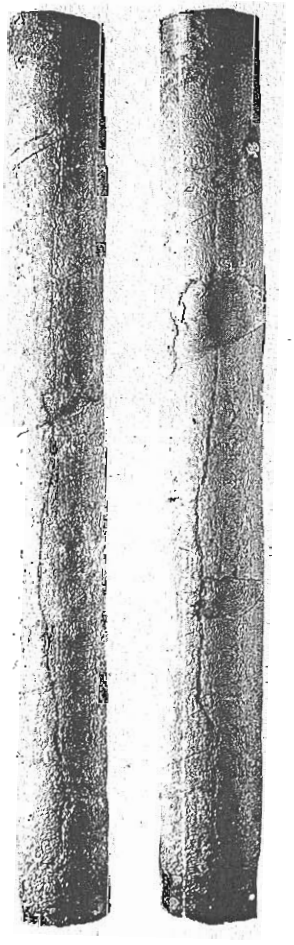

B.

Figure 10.2 Hydrofracting method of measuring stress. *A.* Verrical and horizontal sections of a borehole packer used to isolate a section of the borehole. Fluid pressure is increased between the seals to induce hydrofracture, which occurs at the critical pressure P_c. *B.* Impression of the inside of the borehole following hydraulic fracturing. The impression of the induced extension fracture is clearly visible roughly parallel to the borehole.

several hundred kilometers—much greater than borehole techniques can reach. The radiation pattern of first motions of P waves and the location of earthquake aftershocks indicate, respectively, the sense of shear and the fault orientation at depth (see Box 2.4 and Figure 2.17). The maximum compressive stress $\hat{\sigma}_1$ lies in the rarefraction first-motion quadrant (*not* the compressive first-motion quadrant) perpendicular to the intersection of the fault plane and the nodal plane. The von Mises failure criterion (Figure 9.9) suggests that it bisects the angle between those planes. The orientation is approximate because the von Mises criterion is not necessarily the best one to use, and the mechanism for deep-focus earthquakes is not well understood. First-motion studies do not give reliable information about the stress magnitudes.

Field observation of faults and the slip direction on them can be used, under favorable circumstances, to infer the orientation of the principal paleostresses that caused the faulting. We discuss this very useful technique further in Section 10.10.

10.2 Stress in the Earth

Vertical Normal Stress

We commonly assume that the principal stresses are vertical and horizontal, because they must have that orientation at the horizontal surface of the Earth. A plot of principal stress orientations on a stereonet should therefore show a tight cluster of axes about the center of the net and a distribution of axes around the periphery. Figure 10.3*A* shows, for example, principal stress orientations determined in southern Africa. Although there is some clustering about the center of the net, there is a large amount of scatter, suggesting that the assumption is only a rough generalization.

Another common assumption is that the vertical normal stress should be equal to the overburden, which is determined by the density of the rocks. Figure 10.3*B* shows a set of measurements of the vertical normal stress compared with the overburden stress for a mean rock density of 2700 kg/m^3. In fact, although the overburden stress is a good average of the vertical stresses, there is a great deal of variability, which again warns us that the common assumption is an oversimplification.

Nontectonic Horizontal Normal Stress

In a sedimentary basin that has not been subjected to tectonic deformation, we generally expect the state of stress to be dominated by the overburden. In such a case, the principal stresses should be vertical and horizontal, and the vertical normal stress should be the maximum compressive stress and should be equal to the overburden. The horizontal stress, however, is more difficult to estimate. We can suppose that the sediments in a basin behave as an elastic solid, and that the geometry of the Earth requires that the horizontal Poisson expansion be zero ($\hat{e}_{xx} = 0$). We can then calculate the magnitude of the horizontal stress σ_H that would exactly counteract the Poisson expansion due to the vertical stress σ_V as follows. Form the elasticity equation for $\hat{e}_{xx}$ from Equation (9.5) by changing subscripts z to x and x to z. Then set $\hat{\sigma}_{xx} = \hat{\sigma}_{yy} = \sigma_H$, $\hat{\sigma}_{zz} = \sigma_V$, and $\hat{e}_{xx} = 0$. Solving for the horizontal stress gives

$$\sigma_H = \frac{\nu}{1 - \nu}\sigma_V \tag{10.1}$$

For ν between 0.25 and 0.33, which are common values of Poisson's ratio for rock, this equation implies that the horizontal stress should be only between about a third and half of the vertical stress. The constant $\nu/(1 - \nu)$ is one possible value for the constant κ in

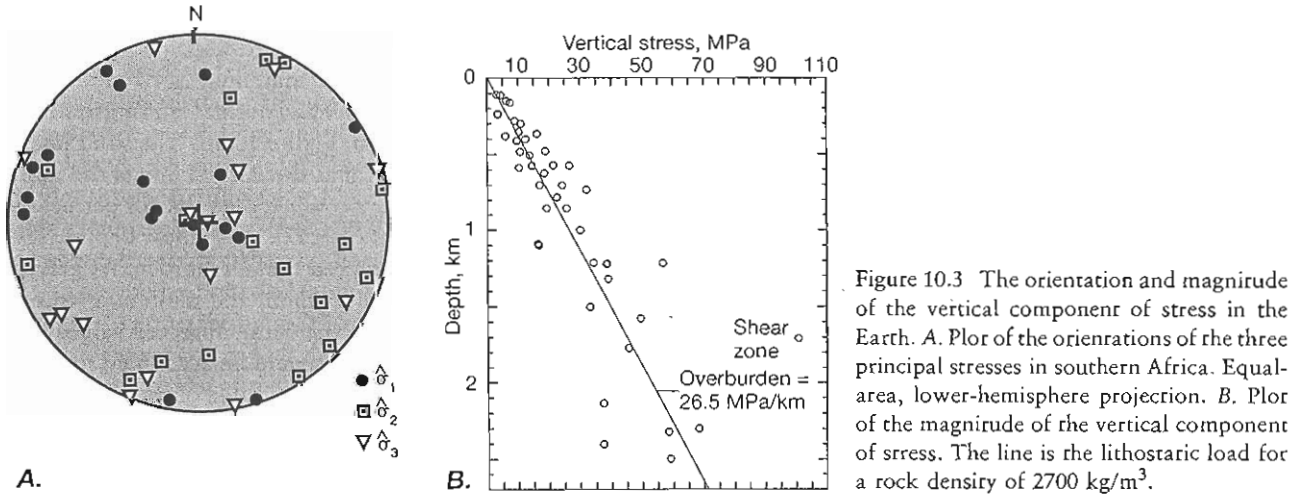

Figure 10.3 The orientation and magnitude of the vertical component of stress in the Earth. *A.* Plot of the orientations of the three principal stresses in southern Africa. Equal-area, lower-hemisphere projection. *B.* Plot of the magnitude of the vertical component of stress. The line is the lithostatic load for a rock density of 2700 kg/m^3.

Equations (8A.2) and (8A.3) (Appendix to Chapter 8) and in Equation (10.3) (Section 10.9).

Figure 10.4 shows the values of the minimum horizontal compressive stress in sedimentary basins in the United States, determined by the hydrofrac technique. For comparison, the different lines indicate the overburden stress, the hydrostatic pressure, and the minimum compressive stress predicted from the Poisson effect for two values of ν. Except for three measurements in granite, the stress calculated from the Poisson effect sttess is too low, indicating that the assumptions we made for the calculation are not realistic.

If we had assumed that rocks were sufficiently ductile so that the flow would eliminate any differential stress, it would be equivalent to assuming that $\nu = 0.5$. In that case, the state of stress would be lithostatic and equal to the overburden ($\sigma_H = \sigma_V = \rho_r g h$). Figure 10.4 shows that this also is not a realistic assumption.

At best, the horizontal normal stress calculated from the extreme values of the Poisson ratio gives maximum and minimum bounds for a nontectonic stress.

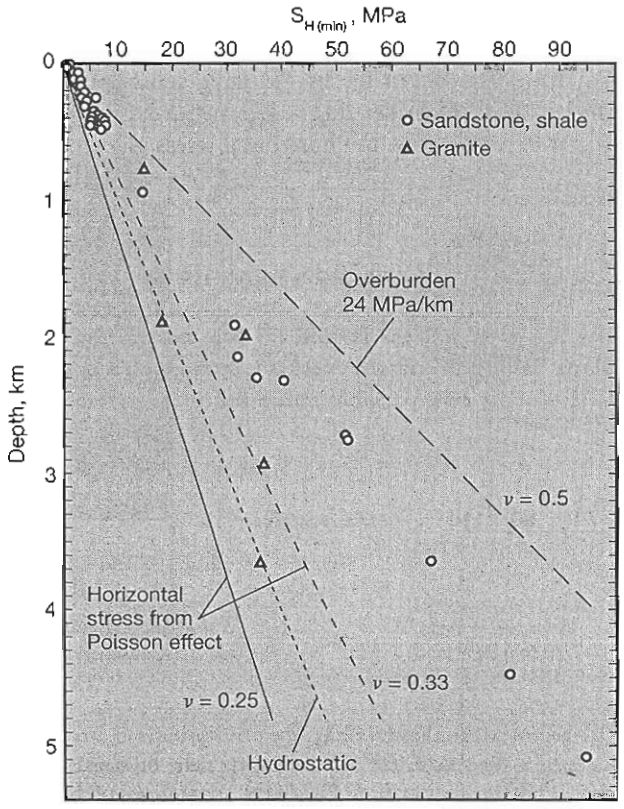

Figure 10.4 The minimum horizontal compressive stress measured by the hydrofrac technique in sedimentary basins in the United States (data points) compared with the overburden pressure, the hydrostatic pressure, and the minimum horizontal stress predicted by the Poisson effect for $\nu = 0.25$ and 0.33.

Tectonic Horizontal Normal Stress

The only constraint we can put on horizontal stresses of tectonic origin is that the differential stress (the diameter of the Mohr circle) must not exceed the strength of the rock. We assume the strength is determined by the Coulomb fracture criterion, which we express as a relationship between the maximum and minimum principal stresses at fracture (Box 9.1 and Equation 9.1.2). For the sake of argument, we also assume that the principal stresses are horizontal and vertical and that the vettical stress is the overburden, although these are not necessarily accurate assumptions. We consider the cases for horizontal tectonic extension and horizontal tectonic compression with a fracture angle $\theta_f = 60°$ and a cohesion $c = 10$ MPa, which give $S = 34.6$ MPa and $K = 3$ in Equation (9.1.2).

For the condition of tectonic extension, the vertical normal stress is the maximum comptessive stress, $\sigma_V = \hat{\sigma}_1$, and we can solve Equation (9.1.2) for the minimum possible value of $\hat{\sigma}_3$. The variation with depth for both the maximum and the minimum principal stresses for this case is shown in Figure 10.5*A* by the solid lines labeled overburden and min $\hat{\sigma}_3$, respectively. For the state of tectonic compression, the vertical normal stress is the minimum compressive stress, $\sigma_V = \hat{\sigma}_3$, and we can solve Equation (9.1.2) for the maximum possible value of $\hat{\sigma}_1$. The variation with depth for both the minimum and the maximum principal stresses is shown for this case in Figure 10.5*A* by the solid lines labeled overburden and max $\hat{\sigma}_1$, respectively.

The predicted strength of the rock is decreased if the effect of pore fluid pressure is taken into account (see Section 9.5). In Equation (9.1.2), the principal stresses $\hat{\sigma}_1$ and $\hat{\sigma}_3$ must be replaced by the effective principal stresses ${}_E\hat{\sigma}_1 = \hat{\sigma}_1 - p_f$ and ${}_E\hat{\sigma}_3 = \hat{\sigma}_3 - p_f$, tespectively. We express the pore fluid pressure as a fraction λ of the overburden, $p_f = \lambda\sigma_V$ (Equation 9.17), and plot the results in Figure 10.5*A* as dashed lines for different values of λ in each of the fields for horizontal extension and horizontal compression.

Measurements of the minimum horizontal stress from an area of subsidence and normal faulting in southetn Africa are shown in Figure 10.5*B*. The solid line is again the overburden, and the dashed line is the minimum possible stress for $\lambda = 0.4$, the value for permeable saturated rock (Equation 9.17). At shallow depths, several values of stress exceed the overburden. At greater depths, the predicted maximum and minimum stresses are better constraints to the data. Observed values falling below the $\lambda = 0.4$ line could be accounted for by a lower value of λ or by a larger value of the cohesion c, which has the effect of moving the stress axis intercept to more negative values.

Note that the plot of minimum values of $\hat{\sigma}_3$ in Figure 10.5*A* indicates that actual tensile stresses (neg-

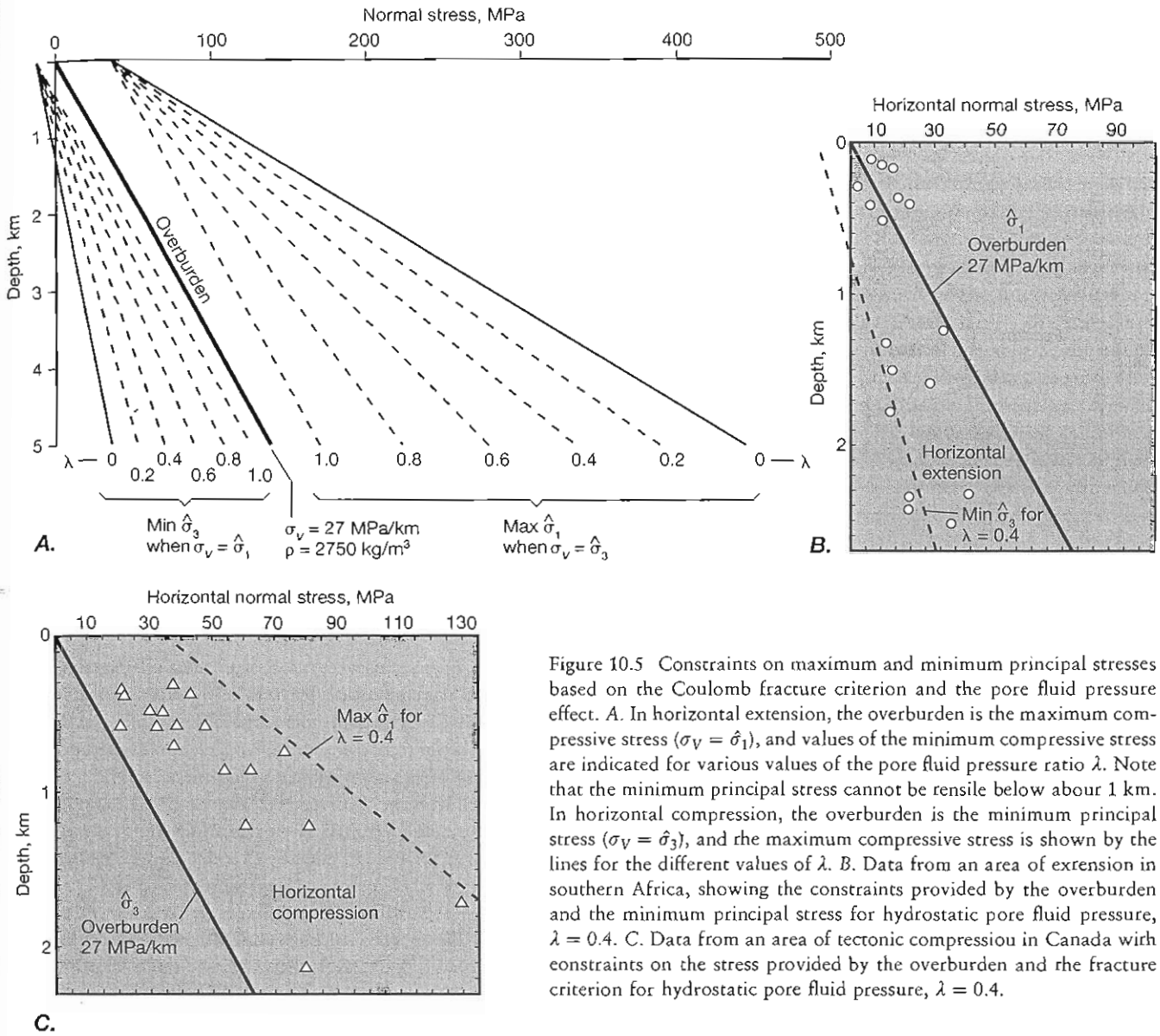

Figure 10.5 Constraints on maximum and minimum principal stresses based on the Coulomb fracture criterion and the pore fluid pressure effect. *A*. In horizontal extension, the overburden is the maximum compressive stress ($\sigma_V = \hat{\sigma}_1$), and values of the minimum compressive stress are indicated for various values of the pore fluid pressure ratio λ. Note that the minimum principal stress cannot be rensile below abour 1 km. In horizontal compression, the overburden is the minimum principal stress ($\sigma_V = \hat{\sigma}_3$), and rhe maximum compressive stress is shown by the lines for the different values of λ. *B*. Data from an area of exrension in southern Africa, showing the constraints provided by the overburden and the minimum principal stress for hydrostatic pore fluid pressure, $\lambda = 0.4$. *C*. Data from an area of tectonic compressiou in Canada with eonstraints on the stress provided by the overburden and rhe fracture criterion for hydrostatic pore fluid pressure, $\lambda = 0.4$.

ative values of the normal stress) cannot exist below a depth of about 1 km. In fact, tensile stresses have not been measured within the Earth at all.

Measurements of the maximum horizontal stress from a region of folding and thrust faulting in Canada are plotted in Figure 10.5*C*. The solid line is the overburden stress, and thc dashed line is the maximum possible compressive strcss for $\lambda = 0.4$. All the measured stresses fall between the two lines.

This mcthod of constraining the differential strcss applies at best to thc upper 15 km to 20 km of the crust, which is the range in which deformation is brittle. Below that, rhe increases in temperature and pressure induce a weakening of the rock because of the onset of ductile deformation processes (see Sections 18.4 to 18.6), and the Coulomb fracture criterion does not predict the strength of the rocks.

Regional Distributions of Stress

Stress orienrations from all over the world measured with the techniques discussed above are summarized in Figure 10.6*A*. The figure shows the location of stress measurements, the orientation of principal stresses, and the type of stress determination. Over large rcgions, there is rcasonable agreement among the different measurement techniques, but the orientations of the principal stresses change substantially even within a single continent. Thcse stressrs reflect major tectonic processes in the Earth and provide important constraints on models of the driving forces for plate tectonics, which must account for the observed stress distribution within the plates, at least to a first approximation.

Figure 10.6*B* presents a more detailed summary of stress orientation measurements in the United States.

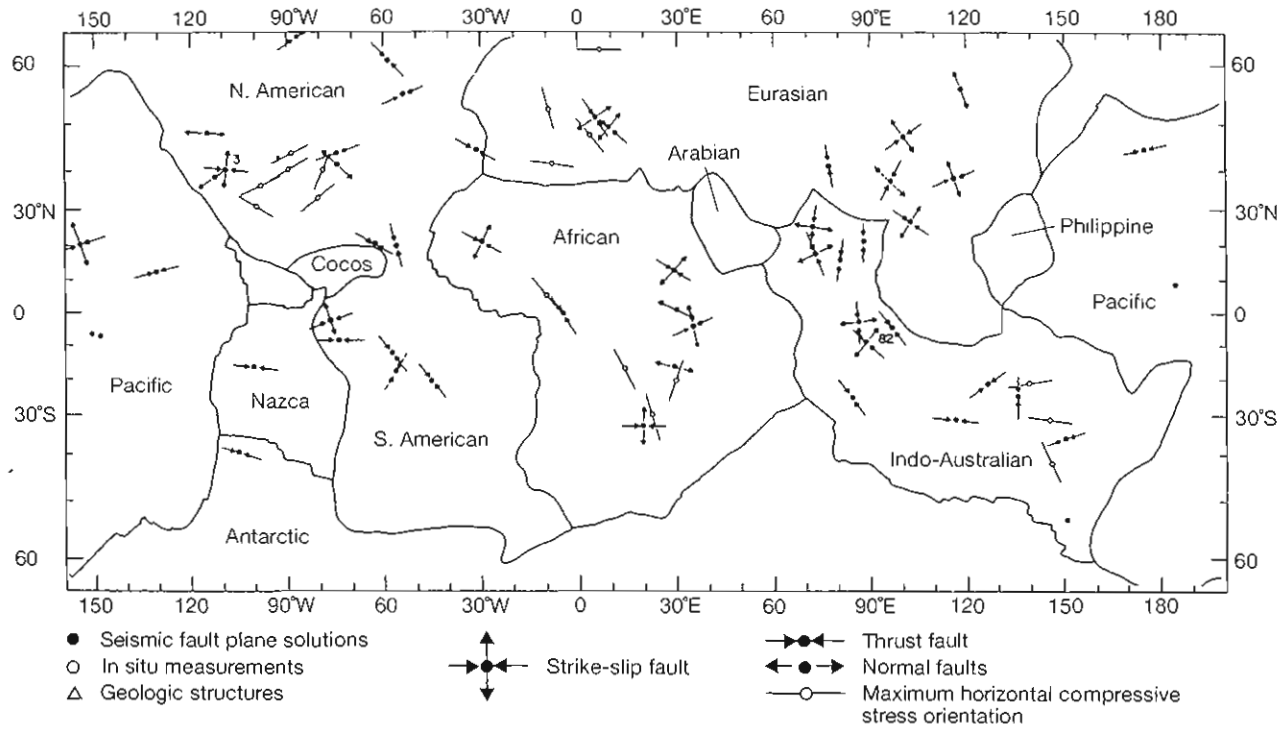

A.

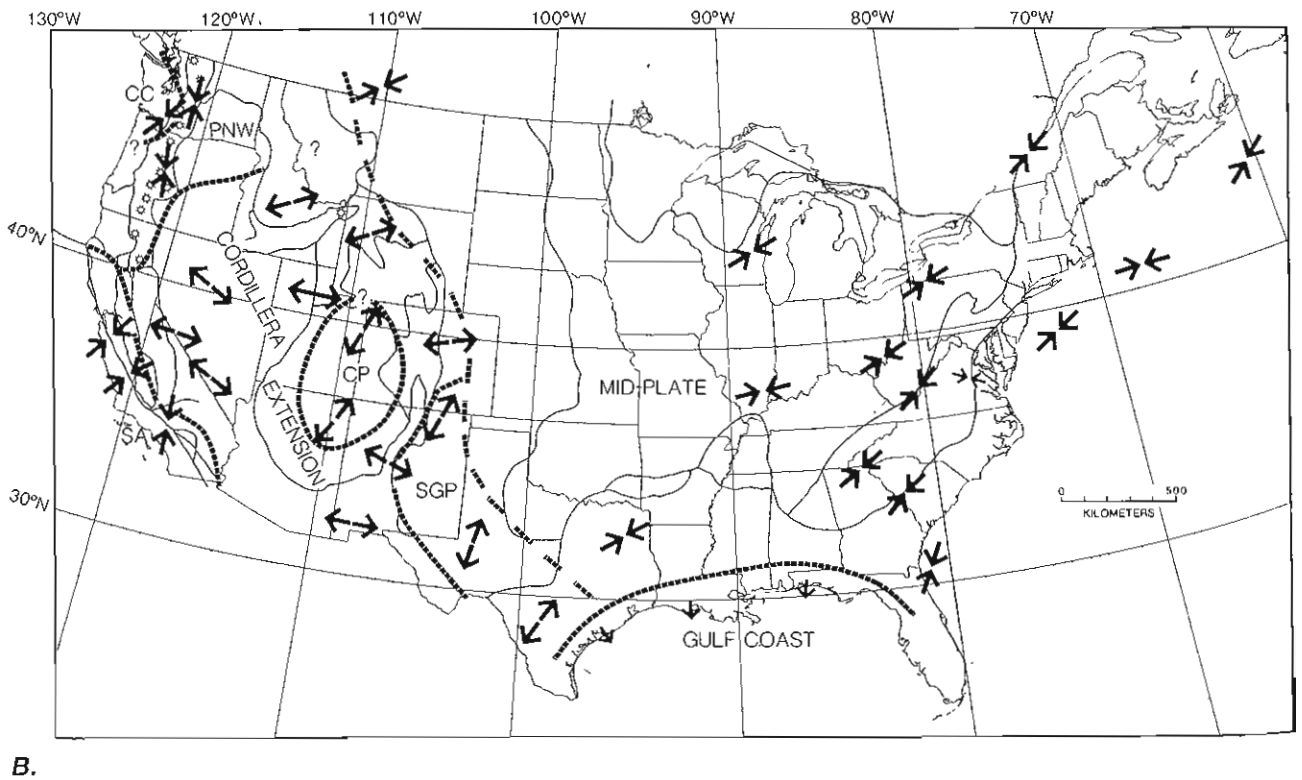

B.

Figure 10.6 Regional stress field determinations. *A*. Worldwide distribution of principal stress orientations. *B*. Stress orientations in the coterminus United States.

The boundaries separate regions of roughly similar states of stress, and to a significant exrent, these regions correspond to geologic provinces in which the structures reflect the different tectonic regimes.

10.3 Mechanisms of Stressing the Earth's Crust

Stress arises in the Earth because of the overburden, the driving mechanisms of plate tectonic processes, horizontal and vertical motions, changes (over space and time) in temperature and pressure, the inhomogeneous mechanical properties of the crust, and pore fluid pressure. Once we understand the mechanisms by which stresses arise, we can begin to understand the possible origin of fractures in the Earth by making models of loading histories and their consequences. In this section, therefore, we examine the mechanisms by which the Earth's crust can be stressed.

The Overburden

Because the overburden stress results from the weight of the overlying column of rock, surface topography affects the stress distribution at depth. The greatet the topographic relief, the greater the magnitude of the effect. The influence of topography on stress dies out with increasing depth and is generally negligible at depths greater than the horizontal length of the topographic feature, which may, however, be considerable.

The overburden may be increased by sedimentation or by tectonic thickening such as thrust faulting; conversely, it may be decreased by erosion or by tectonic thinning such as normal faulting. The resulting change in pressute should cause different amounts of deformation in different types of rocks, because each is characterized by its own elastic constants. If the rocks are constrained to deform the same amounts, however, stresses must be different in each rock type in order to satisfy these constraints.

Driving Processes of Tectonics

Stresses associated with plate motion are one of the major sources of regional stress in the lithosphere. Such stresses may arise from the pull of the down-going slab as it descends in a subduction zone, from the push of a midoceanic ridge associated with its relative topographic elevation above the adjacent sea floor, from the drag between the lithosphere and the underlying asthenosphere as the plates move relative to the underlying mantle, or from the interaction of adjacent plates. The stresses associated with subduction are particularly important ro the formation of structures during collisions involving continents or island arcs with subducrion zones.

Horizontal and Vertical Motions

Bending of the crust and of the lithosphere generates stresses whose extent is comparable to the wavelength of the bending. Plates bend ar subduction zones where the plate entets the trench. Plates bend duting isostatic response to surface loads, such as the huge volume of volcanic rocks of the Hawaiian Islands, the thick accumulations of ice in continental ice sheets, the thick sediments that accumulate in sedimentary basins, and the unloading caused by erosion. Deviatoric tensile stress should develop on the convex side of the bend, and deviatoric compressive stresses on the concave side (Figure 10.7). Bending of lithospheric plates also occurs as they drift from one latitude to another, because the Earth is roughly ellipsoidal in shape, and the surface has a greater curvature (a smaller tadius of curvature) at the equator than at the poles. The plates must bend to accommodate this change in curvature.

Vertical motions, such as tesult from isostatic adjustment, can also induce stresses in rocks. As a segment of the crust is uplifted, for example, it should subtend a constant central angle β. As the radial distance from the Earth's center increases, however, the arc length increases, thereby stretching the rock in both horizontal directions.

Thermal and Pressure Effects

Thermal expansion or contraction of rocks in response to changes in temperature induces stresses in the rocks if they are not free to expand or contract. The stresses must be of sufficient magnitude to counteract the changes in dimension that would be caused by temperature changes in the unrestrained rock. Because different rocks have different coefficients of thermal expansion, a temperature change induces different stresses in two immediately adjacent but different rock types, such as a limestone and a sandstone. Stresses are also induced where different amounts of temperature change occur

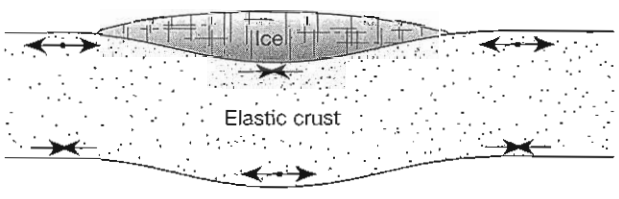

Figure 10.7 Bending of the elastic part of the lithosphere in response ro the loading of a continental ice sheet causes deviatoric eompression on rhe concave sides of rhe bends and deviatoric tension on the convex sides.

in adjacent roeks, such as where a magmatic intrusion cools off while the adjacent country rock warms up.

Because different types of rocks have different elastic coefficients, changes in pressure associated with the addition or removal of overburden induce different amounts of strain under unconstrained conditions. If the deformation is constrained, a differential stress must build up of sufficient magnitude to satisfy the constraints.

Pore Fluid Pressure

Finally, the existence of pore fluid pressure in rocks strongly affects their mechanical response and can cause extension fracturing even under conditions of purely compressive applied stresses (see Section 9.5 and Figure 9.13*A*). High pore fluid pressures can develop simply from the compaction of impermeable sediments, which decreases the pore volume. If this volume is filled with water, and if the water eannot escape from the sediment, then the pore fluid pressure must increase.

Water has a higher coefficient of thermal expansion than sediment, so if the pores are saturated with water that is trapped by impermeable layers, the pore fluid pressure must increase with temperature. This phenomenon is referred to as aquathermal pressuring.

Prograde metamorphic reactions, which occur under conditions of increasing temperature and pressure, are commonly dehydration or decarbonation reactions that release water or carbon dioxide, respectively, into the rock. Most crystalline rocks are highly impermeable, and if these fluids are produced faster than they can migrate away through the rock, the pore fluid pressure must increase. Hydrofractures may be a common feature of metamorphic terranes deep in the crust.

Partial melting during very high-grade metamorphism in deep crustal regions may also create high pore fluid pressure. In such a situation, the first melts to form are fluid-rich and generally of granitic composition. If the fluid cannot escape, the pressure of the melt can become very high. Some veins in the deepest core regions of mountain belts may originate as fractures induced by the fluid pressure of such melts.

10.4 Stress Histories and the Origin of Joints

Given the wide variety of mechanisms for inducing and changing stress conditions in the Earth's crust, it is not surprising that fractures in the crust have numerous possible origins. In this section, we look at possible loading histories that can lead to the formation of joints. Because joints are extension fractures, the tension fracture criterion is relevant to explaining their origin.

For sedimentary basins, we distinguish two principal sets of conditions: those that cause jointing during burial and those that cause jointing during uplift and erosion. The stress path associated with burial followed by uplift is not a reversible path, because the mechanical properties of the material change with time. During burial, the unconsolidated sediments gradually become compacted and lithified and may be affected by tectonic deformation. Thus when rocks are uplifted, they are very different materials from when they were buried, and they have different mechanical properties. This difference affects the way stresses accumulate (see Box 10.1).

All stresses that have been measured directly in the Earth are compressive; true tensile stresses are rare. For extension fractures to form, therefore, two conditions must be met. Pore fluid pressure must be large enough for the effective minimum principal stress to become tensile, and the differential stress must be small enough so that, at the critical pore fluid pressure, extension fractures form (Figure 9.13*A*) rather than shear fractures (Figure 9.13*B*).[1] Values of the tensile strength $|T_0|$ for small rock samples measured in the laboratory vary from a few megapascals for weak sedimentary rocks up to around 40 MPa for crystalline rocks. Widespread planes of weakness in crustal rocks, such as fractures and bedding planes, however, result in very low bulk tensile strengths. Measured differential stresses are generally small and tend to increase slightly with depth, being generally less than 20 MPa near the surface and, at 5 km depth, reaching values of no more than 50 MPa in sedimentary rocks and 70 MPa in crystalline rocks (Figure 10.5). Thus it is probable that hydrofracture in rocks should often result in extension fractures.

Joint Formation During Burial

In tectonically quiescent sedimentary basins, at depths less than about 3 km, measured fluid pressures are generally not greater than hydrostatic pressure, which suggests that flow of fluids through the rock is unrestricted above that level. With increasing depth of burial, flow becomes restricted, and compaction and aquathermal pressuring can increase the fluid pressure more rapidly than the minimum compressive stress increases. Eventually hydrofracture results.

In permeable rocks, the sudden local decrease of pore fluid pressure at the fracture causes a rapid flow of pore water into the fracture. If the sediment is unconsolidated, some of it may be carried into the fracture, producing clastic dikes.

[1] According to the Griffith theory of fracture, the differential stress (the diameter of the Mohr circle) that can cause extension fracturing is limited by $(\hat{\sigma}_1 - \hat{\sigma}_3) < 4|T_0|$, where T_0 is the tensile strength. This is the largest Mohr circle that can be tangent to the parabolic fracture criterion at the vertex of the parabola (see Figure 9.13).

The different mechanical properties of disparate rock types mean that in general they do not fracture at the same time. Consider an interlayered sandstone–shale seqnence in which the overbutden stress is the maximum compressive stress, $\hat{\sigma}_1 = \rho_r g h$. Because the sandstone can support a larger differential stress than the shales, the minimum principal stress $\hat{\sigma}_3$ is smaller in the sandstone than in the shale, and a smaller pore fluid pressure is required to cause hydrofracturing in the sandstone than in the shale (Figure 10.8; see Box 10.1). During burial, therefore, as the pore pressure gradually increases, hydrofractures develop first in the sandstone and do not extend into the shale. When pore pressure in the shale rises sufficiently to cause hydrofracture, the sandstone can also fracture, and fractures can cross rhe lithologic contacts. The extent of a set of joints can therefore be a significant factor in the interpretation of the history of joint development.

Joint Formation During Uplift and Erosion

During uplift and erosion, we assume that the principal stresses are horizontal and vertical and that the vertical srress equals the overburden. The vertical normal stress decreases as the overburden diminishes, and the temperature also decreases. The changes in horizontal stress components during uplift determine whether jointing occuts in this phase of the rock's history. The important factors determining horizontal stresses are the Poisson

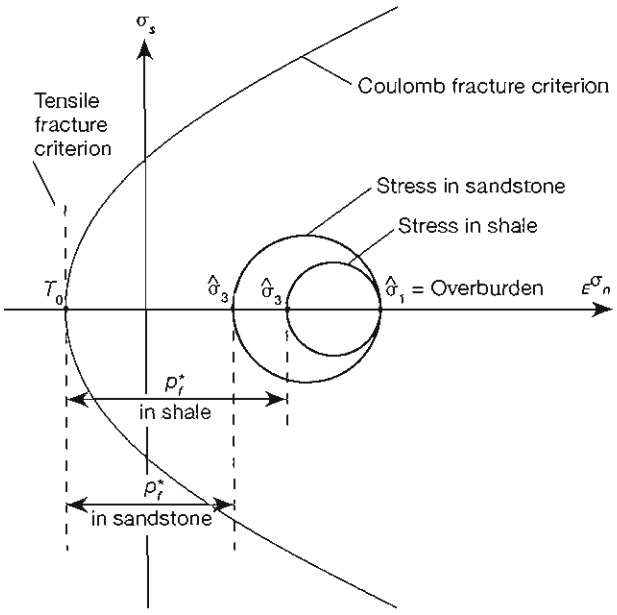

Figure 10.8 Stresses in shale and sand interbeds. The stronger sandstones supporr a larger differenrial stress than the weaker shales. p_f^* is the eritical pore pressure required for hydrofracrure, and it is smaller for rhe sandsrones rhan for the shales.

and thermal effects, which tend to counteract each othet, and bending stresses.

The nplift may be accompanied by doming of the crnst, which creates stresses associated with bending. Without detailed knowledge of the geometry of the uplift, however, these stresses cannot be predicted.

If the rocks behave as an elastic material, the Poisson effect predicts that a decrease in the vertical load will cause expansion in the vertical direction and contraction in the horizontal direction (Figure 9.1*A*). The rocks are not free to change horizontal dimensions, however, so the horizontal components of stress decrease sufficiently to offset exactly the Poisson contraction (Equation 10.1). Starting, for example, from a lithostatic stress at the deepest point of burial, for which $\hat{\sigma}_1 = \hat{\sigma}_2 = \hat{\sigma}_3 = \rho_r g h$, uplifr and erosion would result in a decrease in all components of comprcssive stress, but the horizontal stress would decrease less than the vertical component. Thus the horizontal srress would end up as the maximum compressive stress (see Box 10.1).

Thermal contracrion of the rock associated with a decrease in temperature, however, competes with and commonly overwhelms the Poisson effect. Because the rocks cannot change horizontal dimension, the horizontal compressive stress decreases by an amount that exactly offsets the thermal contraction.

The net effect of most conditions of uplift and erosion is that the horizontal stress becomes the minimum compressive stress, and the vertical stress the maximum compressive stress (see Box 10.1). As long as one of the horizontal *effective* stresses is tensile, however, vertical joints that are normal to that stress component can form. Again, the effect of the pore fluid pressure plays a critical role in producing an effective tensile stress in a compressive stress regime.

The development of one set of vertical joints relieves the effective tensile stress normal to those joints. If the other horizontal principal effecrive srress is tensile, then it becomes the maximum effective tensile stress, and a second set of vertical joints may form orthogonal to the first set. Such systems of orthogonal vertical joints are a common feature, for example, of rhe flat-lying sediments in the midcontinent region of the United States. Dererminarion of the relative riming of joints can be very difficult, however, and this interpretation of the origin of such orthogonal sers of joints is at present only an hypothesis.

Tectonic Joints

If tectonic stresses are imposed on a rock during burial, then compaction and restriction of the pore fluid circulation may occur at shallower depths than is possible under lithostatic loading. The resulting high pore fluid pressures can cause hydrofracturing at depths

Box 10.1 The Effect of Burial and Uplift on Stress

We consider a simple model of the evolution of stress in rocks during burial, lithification, and uplift. The model includes only the overburden, the Poisson effect, and the thermal effect, and we calculate the stress required to maintain a horizontal extension of zero. The change in the maximum and minimum horizontal normal stresses $\Delta\sigma_{H(\max)} = \Delta\sigma_{H(\min)}$, as a function of the changes in vertical stress $\Delta\sigma_V$ and temperature ΔT, is given by

$$\Delta\sigma_{H(\max)} = \Delta\sigma_{H(\min)} = \left(\frac{\nu}{1-\nu}\right)\Delta\sigma_V - \left(\frac{E}{1-\nu}\right)\alpha\,\Delta T \tag{10.1.1}$$

where α is the coefficient of thermal expansion, which gives the extension (Equation 9.1) per degree of temperature change. The first term gives the stress required to counteract the Poisson effect and comes from Equation (10.1). The second term gives the stress required to counteract the thermal effect and comes from the equations of elasticity (similar to Equation 9.5).*

The changes in stress and temperature indicated by the Δ in Equation (10.1.1), are the final minus the initial values, and we can express $\Delta\sigma_V$ and ΔT as a function of the change in depth.

$$\Delta\sigma_{H(\max)} = \Delta\sigma_{H(\min)} = \sigma_H^{(f)} - \sigma_H^{(i)} \tag{10.1.2}$$

$$\Delta\sigma_V = \sigma_V^{(f)} - \sigma_V^{(i)} = \rho_r g(h^{(f)} - h^{(i)})$$

$$\Delta\sigma_V = (25\ \text{MPa/km})\,(h^{(f)} - h^{(i)}) \tag{10.1.3}$$

$$\Delta T = (25°\text{C/km})\,(h^{(f)} - h^{(i)}) \tag{10.1.4}$$

* In Equation (9.5) change subscripts z to x and x to z to obtain the equation for $\hat{\epsilon}_{xx}$. Assume that the two horizontal stress components are $\hat{\sigma}_{xx} = \hat{\sigma}_{yy}$ and that $\hat{\sigma}_{zz} = 0$. Solving for $\hat{\sigma}_{xx}$ gives $\hat{\sigma}_{xx} = [E/(1-\nu)]\hat{\epsilon}_{xx}$. Then set $\hat{\epsilon}_{xx} = -\alpha\,\Delta T$ so that it is the contraction required to cancel out the thermal expansion, that is, it is the negative of the thermal extension.

where the superscripts (f) and (i) indicate "final" and "initial" respectively, and where h is the depth in kilometers. We then substitute Equations (10.1.2) through (10.1.4) into Equation (10.1.1).

With this model, we determine the history of stress for both a sandstone and a shale that are buried as unconsolidated sediments to a depth of 1 km, lithified at the maximum depth of burial, and uplifted back to the surface. The elastic and the thermal expansion constants listed in Table 10.1.1 show that the clay and shale have different mechanical properties, as do the sand and sandstone. This fact ensures that the stress history during burial is different from that during uplift, as shown in Figure 10.1.1.

For the burial, we take $\sigma_H^{(i)} = 0$ MPa, $h^{(f)} = 1$ km, and we solve for $\sigma_H^{(f)}$ by using the constants for sand and clay listed in Table 10.1.1. At a depth of 1 km, the final horizontal stresses on the sand and clay, respectively, are 7 MPa and 25 MPa, and the vertical stress for both is 25 MPa (Figure 10.1.1). For uplift, we use the final horizontal stress from burial as the initial horizontal stress for uplift, $\sigma_H^{(i)} = 7$ MPa or 25 MPa, we use $h^{(i)} = 1$ km and $h^{(f)} = 0$ km, and we use the constants for sandstone and shale from Table 10.1.1. The final horizontal stresses at the surface are -12 MPa and 9 MPa for the sandstone and shale, respectively (Figure 10.1.1).

For the sand in this simple model, the horizontal stress is compressive during burial and is the minimum principal stress; the vertical stress is the overburden and is the maximum principal stress (Figure 10.1.1*A*). Because lithification from sand to sandstone changes the elastic properties of the material (Table 10.1.1), uplift of the sandstone carries it along a stress-depth path of shallower slope than for burial. Thus the horizontal stress decreases more rapidly with decreasing depth, and it actually becomes tensile during

much shallower than 3 km, and the orientation of the joints should reflect the orientation of the principal tectonic stresses. Tectonic stresses may be applied either before or after the formation of burial joints. Because tectonic deformation is commonly accompanied by the formation of a foliation in the rocks (see Chapter 14), the cross-cutting relationships of joints with foliations can be an important element in reconstructing the sequence of deformational events.

Tectonic stresses can, of course, affect rocks during uplift as well as during burial. Such stresses can govern the orientation of new joints by changing the value of one of the horizontal components of stress. If a horizontal stress became the minimum compressive stress as proposed above, and to that were added a horizontal tensile tectonic stress, then vertical joints would form normal to the tectonic stress. If the horizontal tectonic stress were the maximum compressive stress, vertical joints would form parallel ro it.

The Origin of Sheet Joints

As we noted in Chapter 3, sheet joints are subparallel to the topographic surface. We mentioned two mechanisms for their formation: Either the topography controls the orientation of the sheet joints, or the orientation

Table 10.1.1 Mechanical Properties of Sediment During Burial and Uplift[a]

	Burial		Uplift	
	Sand	Clay	Sandstone	Shale
E, in MPa	-1.0×10^3	small	-16.5×10^3	-4.9×10^3
ν	0.21	0.5	0.33	0.36
α, in $°C^{-1}$	10.0×10^{-6}	—	10.8×10^{-6}	10.0×10^{-6}

[a] Data assembled from various sources by Engelder (1985)

uplift. The tensile strength T_0 is exceeded after only about half the overburden has been removed (Figure 10.1.1*A*), at which point joints could form.

The assumption for clay that $\nu = 0.5$ results in all stress components being lithostatic along the stress-depth path for burial (Equation 10.1 and Figure 10.1.1*B*). After lithification, uplift causes a decrease in the horizontal stress, but this decrease is less than that of the overburden. Thus the horizontal stress remains compressive throughout the history and is the maximum principal stress during uplift (Figure 10.1.1*B*).

Different lithologies therefore can have very different stress histories in response to the same externally applied conditions, and the same fractures do not necessarily develop in all rock types, even in the same location.

Tensile stresses have not been measured in rocks, lithification is not likely to occur only at the greatest depth of burial, and we have neglected the effects of pore fluid pressure, so this model is oversimplified. It does, however, illustrate some of the variability that is inherent in the evolution of stress at depth in different rocks.

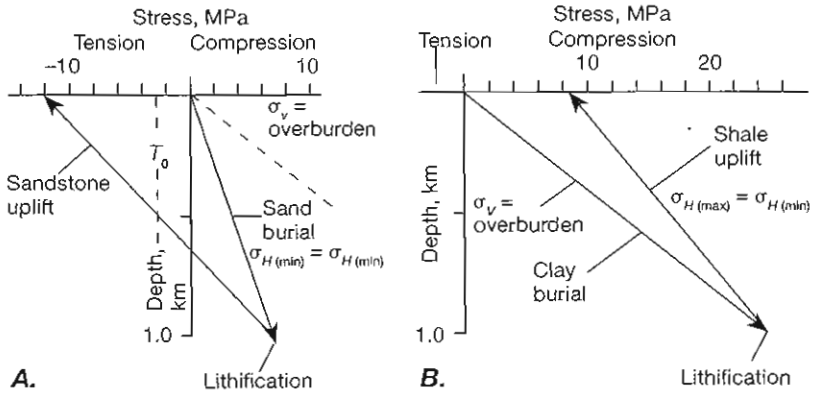

Figure 10.1.1 Stress histories during burial as a sedimenr, followed by lithification and uplift as a rock for (*A*) sand/sandstone and (*B*) clay/shale. The graphs are constructed by using the physical properties from Table 10.1.1.

of the sheet joints is controlled by preexisting stresses in the rock, and the joints affect the evolution of the topography.

Under some circumstances, the maximum compressive stress can remain horizontal and the minimum compressive stress vertical during uplift, as might result if a tecronic compression were applied. As the verrical srtess approaches zero, horizontal joints could propagate in a manner similar to longitudinal splitting. The topography would affect the local orientation of the stress field, because the topographic surface is a free surface that must be a principal surface of stress. Thus the principal stresses locally must be perpendicular or parallel to the topography. This model predicts that the joints should tend to parallel topography.

The alternative hypothesis posits that topography is controlled by the orientation of the joints, which are in rurn the result of residual stresses in the rock. For example, in a plutonic igneous body, cooling at depth concentric with the boundary of the pluton could produce residual thermal stresses within the body with the maximum compressive stress ($\hat{\sigma}_1$) subpatallel to the boundary. As the minimum compressive stress decreases toward zero during uplift, sheet jointing could develop by longitudinal splitting; the orientations of the joints would reflect the shape of the boundary or cooling surfaces in the pluton. Subsequent erosion is controlled by the orientations of rhe joints. The interpretation of sheet joints is nor clear-cut, and borh hypotheses could be correct in different cases.

The Origin of Columnar Joints

The polygonal fracture patterns, or columnar joints, that are common features of many igneous extrusions and shallow intrusions probably resnlt from thermal stresses set up by unequal cooling and thermal contraction between the igneous body and the country rock. After solidificarion, the higher temperature of the igneous rock means that its thermal contraction wonld be considerably greatet than that of the adjacent country rock if the contact were free to slip. A welded contact makes any relative displacement between the two rock masses impossible. In this case, as the two rocks cool, stresses build up on both sides of the contact sufficient to prevent displacement along the contact. Normal stress components that are parallel to the contact are tensile in the igneous rock, preventing it from contracting as much as thermal contraction would require; these stress components are balanced by a compressive stress in the country rock, which forces it to contract more than thermal contraction would require. In general, the tensile stresses in the igneous rock become oriented parallel to the isothermal surfaces during cooling. Because rocks are weaker in tension than in compression, the igneous rocks tend to form tensile fractures perpendicular to the surfaces of equal temperature.

The origin of the hexagonal shape of the columns is not well understood. More than one set of fractures is required to relieve the tensile stress in two orthogonal directions. Such a system of fractures can fill a volume with close-packed fracture-bounded prisms if the prism cross section is triangular, rectangular, or hexagonal. Of these, the hexagonal prisms have the smallest fracture surface area per unit volume of prism. Thus fracture-bounded prisms with a hexagonal cross section require less energy to produce than other prism shapes, and this form of columnar joint is dominant. In principle, however, two sets of fractures should suffice to relieve tensile stresses in two orthogonal directions. Consequently, we do not at present understand the mechanism of development of the three sets of tensile fractures that define the hexagonal prisms.

A similar process must account for the development of hexagonal mud cracks, which form during the desiccation and associated contraction of the surface layers of mud.

10.5 The Spacing of Extension Fractures

The regular spacing of joints and the dependence of that spacing on layer thickness (Figure 3.11) are characteristics that any proposed mechanism of formation must account for. Several explanations have been suggested, but there is no definite proof which, if any, is correct.

One hypothesis that has been proposed to explain the characteristic fracture spacing involves the pore fluid pressure. When a fractnre forms, the pore fluid pressure in the neighborhood of the fractnre decreases as pore fluid flows into the open fractnre. As the pore fluid pressure declines, the effective Mohr circle moves away from the failure criterion, so further fracture in the vicinity of the initial fracture is impossible. A second fracture can form in the rock only beyond the zone of reduced pore pressure, thereby defining the minimum spacing for the formation of hydrofractures. This distance must depend on the permeability of the rock, so highly permeable rocks should have a larger fracture spacing than less permeable rocks.

Layers can also be fractured by the contact forces imposed by adjacent layers. To illustrate this process, consider three layers with welded contacts (Figure 10.9). Suppose that upon uplift, the two outside layers tend to extend more than the central layer. The normal component of stress parallel to the layers is compressive in the outside layers and tensile in the central layer. The force F_t resulting from the tensile stress across the thickness of the layer must balance the forces F_s exerted by the shear stresses along the surfaces of the layer: $F_t = 2F_s$. F_s increases with the length ℓ of the layer. Thus the spacing of the extension fractures that can form within the layer is determined by the length of layer necessary to build up a tensile stress equal to the fracture strength, $F_t = T_0$. For a thieker layer, the fracture spacing should be larger because the force required to fraeture the layer is larger. In principle, this also must be the type of process involved in the formation of columnar joints.

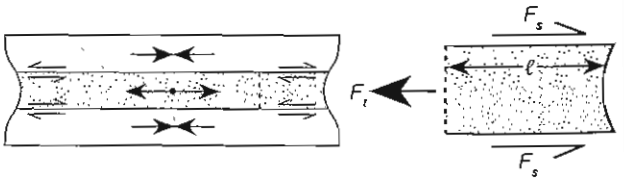

Figure 10.9 Changes in pressure, stress, or temperature can induce stresses in a layer imbedded in a rock of a differenr type if the coefficients of thermal expansion or elasric constants differ berween layer and matrix. In a three-layer sequence, if the central layer tends to expand less rhan the layers on either side, the central layer will be in a srate of tension. The force created by the shear stress on the boundaries of the central layer increases with length of the boundary ℓ; ℓ must be long enough so thar the rensile force in the layer divided by irs cross-sectional area equals the tensile strength. That disrance represents the smallest possible spacing of rhe fractures.

If a tensile fracture develops, the tensile stress normal to the fracture surface is relieved in the neighborhood of the fracture. In an isolated homogeneous elastic body, the stress relief is negligible at a distance away from the crack equal to about five ro ten times the crack depth. Beyond that distance, then another crack may develop. If fracture depth is limited by the thickness of a layer, this relationship suggests that fracture spacing should vary with layer thickness, as is indeed observed. Fracture spacing, however, is usually much less than that predicted by this relationship (Figure 3.11), indicating that this mechanism is not the dominant one.

10.6 Distinguishing Extension Fractures from Shear Fractures

It is often difficult to tell the difference between fractures that have formed as extension fractures and those that have formed as shear fractures, unless some distinguishing characteristic of the mode of formation is present.

The presence of plumose structure on the fracture surface is clear evidence of formation by extension fracturing. Lack of any offset, even down to the microscopic scale, is also clear evidence of extension fracturing.

The presence of pinnate fractures along a fracture is good evidence that the fracture originated as a shear fracture. Pinnate fractures may be extensional cracks that tend to form approximately parallel to the maximum compressive stress. They may also be secondary shear fractures that possibly form at Coulomb fracture angles under locally rotated orientations of the principal stresses relative to the main shear fracture. The orientation of such fractures is uot necessarily a reliable indication of their origin. Fractures that display ridge-aud-groove lineations (see Figure 4.8*A*, *B* and Section 14.6, Figure 14.6*A*, *B*) also must have formed as shear fractures. Such features, however, commonly are not present or are not easily observed on all shear fracture surfaces.

The ambiguity in the interpretation of fracture origin is particularly troublesome for rhose fractures along which there is shear displacemeut. Such fractures may originate as shear fractures, or they may be extension fractures that are subsequently reactivated as shear planes. Reactivated fractures could even have mineral fiber slickenside lineatious (see Chapter 14). On shear fractures that have a very small displacement, however, slickenside lineatious might not develop.

The augular relationship between sets of fractures in rocks is nor diagnostic of the origin of the fractures, although many interpretations in the literature assume otherwise. Two sets of fractures intersecting in an acute angle often are interpreted to be conjugate shear fractures, and sets of three fractures in which oue set bisects

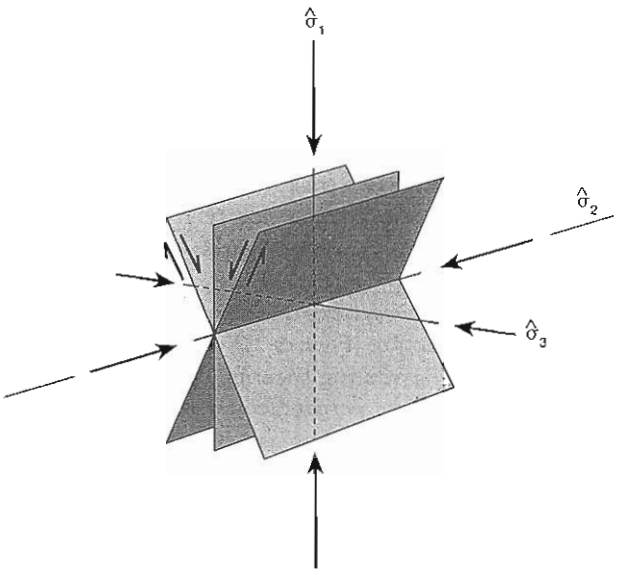

Figure 10.10 Principal stresses inferred from fracture orientations. The maximum compressive stress $\hat{\sigma}_1$ bisects the acute angle between conjugate shear planes; intermediate compressive srress $\hat{\sigma}_2$ is parallel to the inrersection line of the conjugate shear planes; rhe minimum compressive stress $\hat{\sigma}_3$ bisecrs the obtuse angle between rhe conjugate planes. The acure angle between conjugate shear planes is bisecred by an extension fracture.

the acute angle between the other two are interpreted as sets of conjugate shear fractures bisected by an extension fracture. On the basis of the Coulomb fracture criterion and the tensile fracture criterion, the principal stresses are inferred to have had the following orientation with respect to the fractures (Figure 10.10): The maximum compressive stress $\hat{\sigma}_1$ bisects the acure angle between the conjugate shear fractures and parallels the extension fracture; the intermediate priucipal stress $\hat{\sigma}_2$ parallels both the line of intersection of rhe conjugate shear fractures and the extension fracture itself; and the minimum compressive stress $\hat{\sigma}_3$ bisects the obtuse angle between the conjugate fractures and is perpendicular to the extension fracture.

Interpreration of the origin of fractures ou the hasis of their relative orientations, however, is unjustified without indepeudent evidence of the nature of rhe fractures and their relative times of formation. In several well-documented examples, careful investigation of the relative timing of joints has revealed that all the fractures forming a pattern similar to rhat expected for conjugate shear fractures are in fact extension fractures that developed at differeut times and under rhe influence of different orieutations of stress (Figure 3.12). Thus all interpretations in which fracture angle is cited as the only evidence for a shear fracture origin should be regarded with suspicion.

10.7 Fractures Associated with Faults

The fractures that are parallel and conjugate to faults (Figure 3.16) may represent conjugate shear fractures corresponding to the two fracture orientations predicted by the Coulomb fracture criterion (Figure 9.4*B, D, E*). In such a case, the approximate stress orientations are as shown for the conjugate shear planes in Figure 10.10.

Many pinnate fractures that are arrayed *en echelon* along a shear fracture (Figures 3.7 and 4.16*A*) form as extension fractures during shearing, and they are oriented approximately perpendicular to the minimum compressive stress when they form. Some pinnate fractures may also originate as secondary shear fractures such as the *R* Riedel shears (Figures 9.8 and 4.16*C, D*) or the *P* secondary shears (Figures 9.8 and 4.16*E, F*). The acute angles between the fault and both the extension fractures and the *R* Riedel shears point in the direction of relative motion of the fault block containing the secondary fractures. This fact accounts for the sense-of-shear criteria discussed in Section 4.3 (Figure 4.16).

The relationship of gash fractures to the associated shear zone is comparable to that of feather fractures and can be accounted for by assuming the gash fractures form as extension fractures perpendicular to the minimum compressive stress $\hat{\sigma}_3$ (Figure 10.11*A*). The gash fractures, however, may be rotated by ductile deformation during or after formation (Figure 3.8). Gash fractures that initiate at different times during the ductile shear should show different amounts of rotation (Figures 10.11*B* and 3.8). Because the minimum compressive stress $\hat{\sigma}_3$ is normal to any unrotated part of the gash fracture, either the tips of the sigmoidal fractures or the latest-formed fractures provide the best estimate of the stress orientations.

In some cases, *en echelon* gash fractures occur parallel to a conjugate shear zone, an orientation that is not accounted for by this analysis (Figure 3.8). Such orientations may be consistent with the fracture criteria we have discussed and may record locally rotated stress axes. Their geometry may be better accounted for, however, by assuming the fractures form perpendicular to the direction of greatest incremental extension, a possibility we discuss further in Section 17.4. In other cases, each gash fracture may have been completely rotated by ductile deformation, or the set of fractures may have formed as hybrid shears, which have components of both extension and shear across their surfaces (Figure 9.9*B*).

A word of caution is in order concerning the use of fracture orientations to infer the orientations of the principal stresses. Not all fractures near faults form at the same time as the faults. Fractures that predate a fault may actually influence its orientation, because they

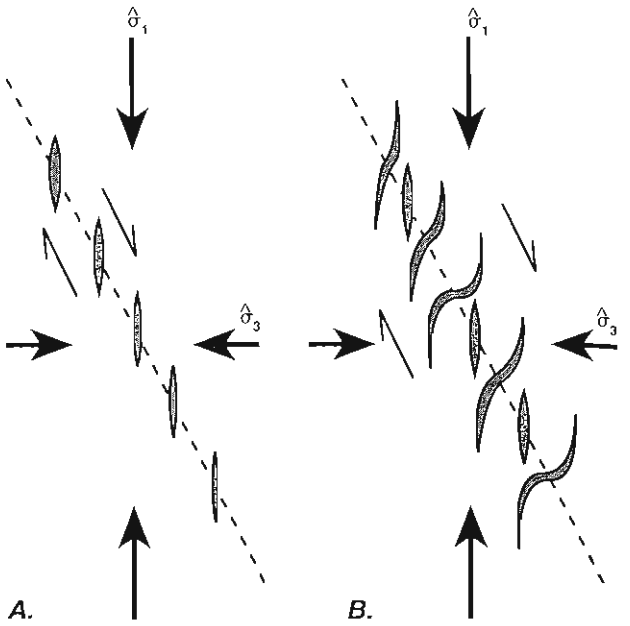

Figure 10.11 Exrension fracture model for the formation of gash fractures. *A*. Gash fractures form an *en echelon* array along a shear zone with each fracture perpendicular to the minimum compressive stress. *B*. Ductile shearing along the shear zone rotates the central portions of the fracrures, leaving a sigmoidal fraeture with rhe tips of the fractures perpendicular to the minimum compressive stress $\hat{\sigma}_3$. Fractures formed at different times during the ductile shearing show different amounts of rorarion, and the smallest, youngest fraetures may not be rorared at all.

are preexisting planes of weakness that give the rock a mechanical anisotropy. Such anisotropies are common and can lead to fractures at orientations different from those predicted by the Coulomb fracture criterion. On the other hand, fractures can postdate an adjacent fault and can have an orientation totally unrelated to it.

10.8 Fractures Associated with Folds

The fracture orientations associated with folds (Figure 3.17) have been interpreted as sets of conjugate shear fractures with or without a set of extension fractures (Figure 10.10). This interpretation seems to be based largely on the relative orientations of the different fracture planes, which in the last section we argued is not a reliable criterion. Some studies of fractures associated with folds, in fact, have found that at least some of the fractures existed in the rocks before the folding.

On the other hand, because the orientation and magnitude of stresses in layers undergoing folding vary radically, both from one place to another in the fold and through time as the fold develops, it is possible ro account, at least qualitatively, for most of the observed fracture orientations.

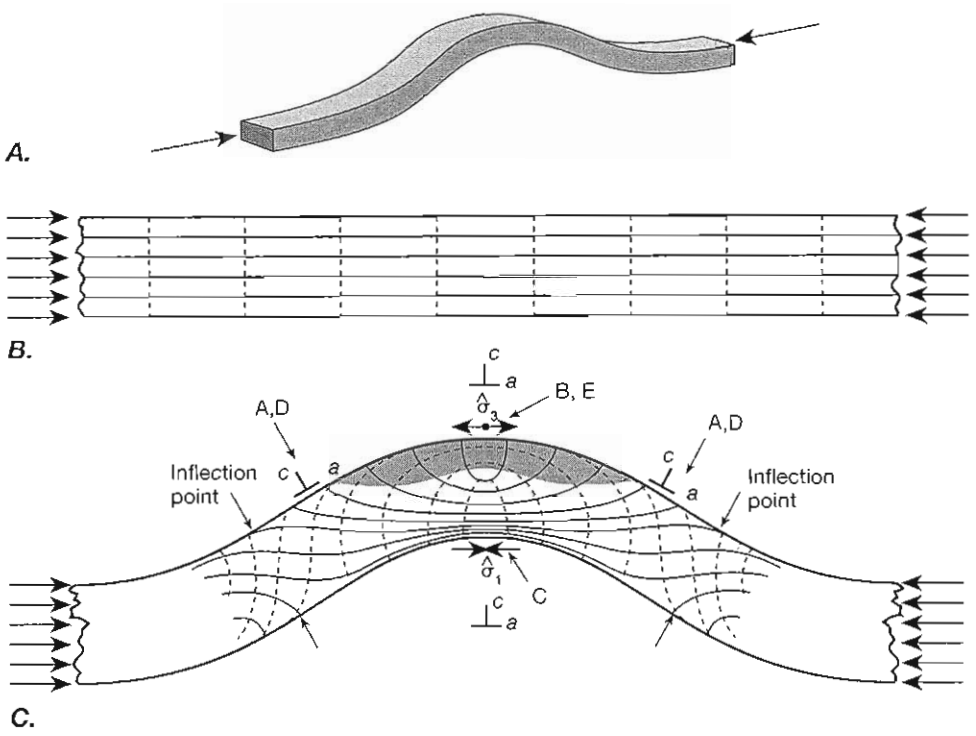

Figure 10.12 Stress distribution in a bar of gelatin undergoing buckling by layer-parallel compression. *A*. Perspective view of the folding experiment. *B*. Stress trajectories in the bar before folding. Solid lines parallel the maximum compressive stress $\hat{\sigma}_1$; dashed lines parallel the minimum compressive stress $\hat{\sigma}_3$. *C*. Stress trajectories in the bar after folding. The shaded area shows where the layer-parallel normal stress compouent is tensile. The letters A through E show locations where different fracture orientations can develop; they correspond to the fracture patterns shown in Figure 3.17 and listed in Table 10.1. Fracture patterns shown in Figure 10.10 oriented with respect to the reference axes *a, b,* and *c* as indicated in Table 10.1 can account for the observed fracture patterns.

Figure 10.12 shows the evolution of stress in an elastic layer folded by layer-parallel compression (Figure 10.12*A*).[2] The lines in Figure 10.12*B* and *C* are stress trajectories, which are everywhere parallel to the principal stresses. Solid lines are trajectories for the maximum principal stress $\hat{\sigma}_1$, and the dashed lines are the trajectories for the minimum principal stress $\hat{\sigma}_3$. The closer the trajectories are to one another, the greater the magnitude of the stress. Before the bar buckles (Figure 10.12*B*), the maximum principal stress is everywhere parallel to the length of the bar, and the minimum principal stress is everywhere perpendicular to the top and bottom of the bar. After buckling (Figure 10.12*C*) the stress orientations are more complex. The maximum principal stress on the concave side of the fold is roughly parallel to the bar and considerably larger than the applied stress, but on the convex side it is at a high angle to the bar. The minimum principal stress on the convex side is parallel to the bar and is actually a tensile stress in the shaded area.

The important points to emphasize in this example are that the orientations of the principal stresses change through time during the buckling process and that the magnitudes—and even the signs—of the principal stresses also change. The existence at the same place of different stresses at different times, and the existence at the same time of different stresses in different places in the fold, can account for the variety of fractures that are observed.

Table 10.1 summarizes the interpretation of the different observed fracture sets (Figure 3.17) in terms of the states of stress that develop during folding (Figure 10.12). The labels of the different fracture sets A through E correspond to the same labels in Figure 3.17 and Table 10.1, and they are used in Figure 10.12*C* to indicate the locations on the fold where the different fracture sets are commonly found. The reference axes *a, b,* and *c* are defined in Table 10.1 and Figure 3.17 and shown in

[2] The experiment was performed on a bar of gelatin illuminated from behind by plane polarized light. Because gelatin is a "photoelastic" material, it rotates the plane of polarization by an amount proportional to the elastic strain. By observing the bar through a polarizer set perpendicular to the original plane of polarization, one can determine the amount of rotation of the polarized light and interpret it in terms of the strain magnitude, which, by the equations of elasticity, is proportional to the magnitude of the stress.

Table 10.1. Stress Interpretation of Fractures in Folds

Fracture set[a]	Principal stress parallel to reference axes[b]			Time of formation[c]	Place of Formation
	a	*b*	*c*		
A	$\hat{\sigma}_1$	$\hat{\sigma}_3$	$\hat{\sigma}_2$	before folding	throughout fold
B	$\hat{\sigma}_3$	$\hat{\sigma}_1$	$\hat{\sigma}_2$	during folding	convex areas of max curvature
C	$\hat{\sigma}_1$	$\hat{\sigma}_2$	$\hat{\sigma}_3$	during folding	concave areas of max curvature
D (conjugate pair)	$\hat{\sigma}_1$	$\hat{\sigma}_3$	$\hat{\sigma}_2$	before folding	throughout fold
bc fractures	$\hat{\sigma}_3$	$\hat{\sigma}_1$	$\hat{\sigma}_2$	during folding	convex side
E	$\hat{\sigma}_3$	$\hat{\sigma}_2$	$\hat{\sigma}_1$	during folding	convex areas of max curvature

[a] The letters correspond to the fracture sets shown in Figure 3.17 and to the locations around the fold shown in Figure 10.12C.
[b] Here c is normal to bedding; *a* and *b* are in the plane of the bedding; *b* is parallel to the fold axis; *a* is normal to *b* and *c* (see Figures 3.17, 10.12C).
[c] In general, "before folding" corresponds to the stress state in Figure 10.12*B*, and "during folding" corresponds to the stress state in Figure 10.12C.

Figure 10.12C, where *b* is everywhere perpendicular to the plane of the diagram.

By orienting the principal stresses and the fracture planes in Figure 10.10 parallel to the reference axes as indicated in Table 10.1, we can account for all the fracture orientations commonly associated with folds in terms of Coulomb shear fractures or extension fractures (Figure 3.17). Note that some fractures (sets A and D) are formed in the stress field that exists before folding (Figure 10.12*B*), and others (sets B, C, E and bc fractures) are formed in the stress field that exists during folding (Figure 10.12C); that some fracture sets that formed at different times occur in the same places; and that the different stresses that exist in different places at the same time during folding account for different fracture sets (for example, sets C and E). The difference between sets B and E and between sets A and C is that the stresses parallel to *b* and *c* exchange positions, presumably depending on local deformation in the direction parallel to *b*.

The interpretation of fractures associated with folds is currently in need of considerable study. We discuss the stress field associated with folding in more detail in Chapter 20.

10.9 Stress Distributions and Faulting

Anderson's Theory of Faulting

The Coulomb fracture criterion provides a useful theoretical explanation for the threefold classification of faults into normal, thrust, and strike-slip faults. This explanation, called Anderson's theory of faulting after the British geologist, E. M. Anderson, who proposed it, depends on the fact that the surface of the Earth is a free surface which can support no shear stress. It must therefore be a principal plane of stress, and at the surface the principal stresses must be normal and parallel to the surface. The Coulomb criterion requires that shear fracture planes contain the intermediate principal stress $\hat{\sigma}_2$ and that the fracture plane angle α_f between the fracture plane and the maximum compressive stress $\hat{\sigma}_1$ be less than 45° (Figures 9.4*B, D, E,* 9.5, and 9.6). The type of fault that develops in a given situation depends on which of the three principal stresses is vertical.

The various possibilities are illustrated diagrammatically in Figure 10.13, where we assume a fracture plane angle of $\alpha_f = 30°$. If the maximum compressive stress $\hat{\sigma}_1$ is vertical, the faults that form should have dips of 60°, and the sense of shear should be hanging-wall-down (Figure 10.13*A*); these are characteristics of normal faults. If the minimum compressive stress $\hat{\sigma}_3$ is vertical, the faults should dip at 30°, and the shear sense should be hanging-wall-up (Figure 10.13*B*); these are characteristics of thrust faults. If the intermediate principal stress $\hat{\sigma}_2$ is vertical, faults should be vertical with horizontal shear directions (Figure 10.13C); these are characteristics of strike-slip faults.

The stress orientations measured in the Earth in regions of active tectonics are generally consistent with this interpretation. For example, the Basin and Range province in Nevada is characterized by roughly north-south–oriented normal faults (Figure 5.10). The minimum horizontal stress is oriented approximately east-west (Figure 10.6*B*), which is consistent with the maximum compressive stress being vertical and thus with the requirements of Anderson's theory for normal faults. The tectonics of the Himalayas are characterized by north-south–directed thrusting. Near the northern

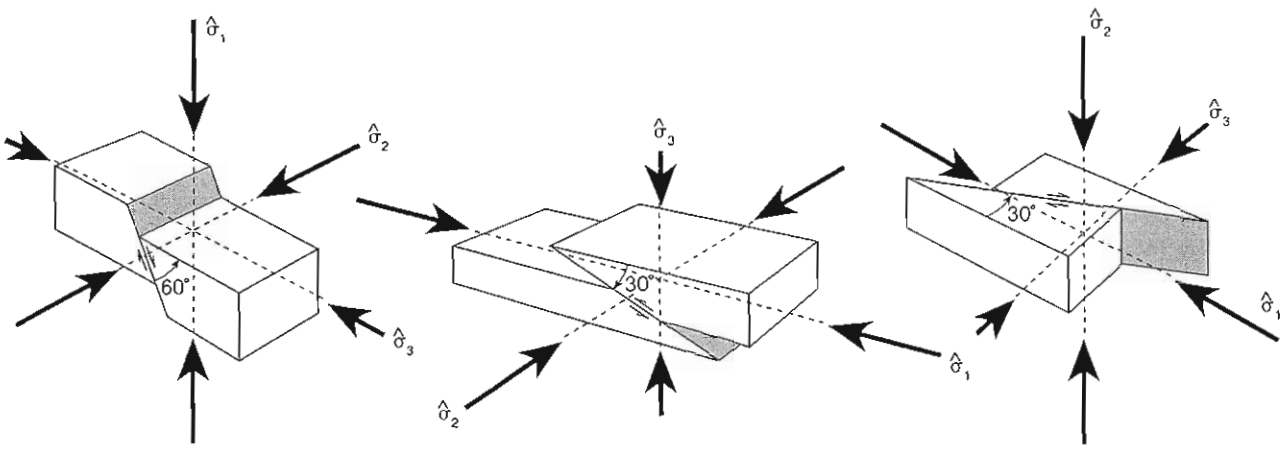

Figure 10.13 Anderson's theory of faulting, showing the relationship between the orientation of the principal stresses and the different ideal fault types. *A*. Normal fault with maximum compressive stress $\hat{\sigma}_1$ vertical. *B*. Thrust fault with minimum compressive stress $\hat{\sigma}_3$ vertical. *C*. Strike-slip faulr with intermediate compressive stress $\hat{\sigma}_2$ vertical.

boundary between the Indian and Asian plates, the maximum compressive stress is oriented approximately north-south (Figure 10.6*A*), which is consistent with the minimum compressive stress being vertical and thus with Anderson's model for thrust faults. Right-lateral strike-slip motion occurs along the northwest-southeast–oriented San Andteas fault in California (Figure 7.2*A*). The maximum compressive stress measured in this atea is oriented roughly north-south (Figure 10.6*B*), consistent with the intermediate compressive stress being vertical as required by Anderson's theory for strike-slip faults. In this case, however, the fault is at a much higher angle to the maximum compressive stress than Anderson's theory would predict. Thus the shear stress on the fault is much lower than expected, which may result from high pore fluid pressure along the fault.

Faulting and the Distribution of Stress with Depth

The Coulomb fracture criterion provides a concise explanation for rhe existence of the three major types of faults observed at the Earth's surface. Strictly speaking, however, it applies only near the surface of the Earth, and it assumes strictly planar faults in isotropic material. Most faults are curved and are not just eonfined to the shallow parts of the crust. In addition, the principal stresses may not be parallel to the horizontal and vertical directions.

Thus it is of interest to examine the possible orientation of the stress field with depth. To investigate this question, we isolate a block of the Earth's crust and consider the distribution of stresses along the boundaries of the block and within it.

We begin by considering the stresses on rock that arise only from the overburden. The vertical normal stress σ_{33} at any depth x_3 in the block is simply the overburden,

$$\sigma_{33} = \rho_r g x_3 \tag{10.2}$$

where ρ_r is the average density of the rock, g is the acceleration due to gravity, and x_3 is the depth (positive values for depth below the surface). The corresponding horizontal stress is equal to a fraction κ of the vertical stress,

$$\sigma_{11} = \kappa \rho_r g x_3 \tag{10.3}$$

where κ is a factor less than 1 rhat depends on the effective Poisson ratio of rhe rock (see Section 10.3 and Equation 10.1).

Because no shear stresses exist at the surface and none are applied to any other surface of rhe block, the principal planes of stress must be parallel and perpendicular to the sides of the block. In other words, the maximum compressive stress $\hat{\sigma}_1 = \sigma_{33}$ is everywhere vertical, and the minimum compressive stress $\hat{\sigma}_3 = \sigma_{11}$ is everywhere horizontal.[3] The stress trajectories, which are lines everywhere parallel to the orientations of these principal stresses, are horizontal and vertical throughout the block. The srate of stress arising only from the overburden is often called the standard state. We discuss various faulting situations by superimposing additional stresses on the standard state.

Consider, first of all, superposition of a tectonic horizontal compressive stress, adequate to cause faulting, on the standard state (Figure 10.14). In the figure, a supplementary horizontal compressive stress K is added to the standard state. If the added stress is suf-

[3] Remember that the principal axes are always numbered such that the principal stresses are $\hat{\sigma}_1 \geq \hat{\sigma}_2 \geq \hat{\sigma}_3$. In cases such as this, therefore, the nnmbering of the principal coordinate axes may be different from that of the general coordinate axes.

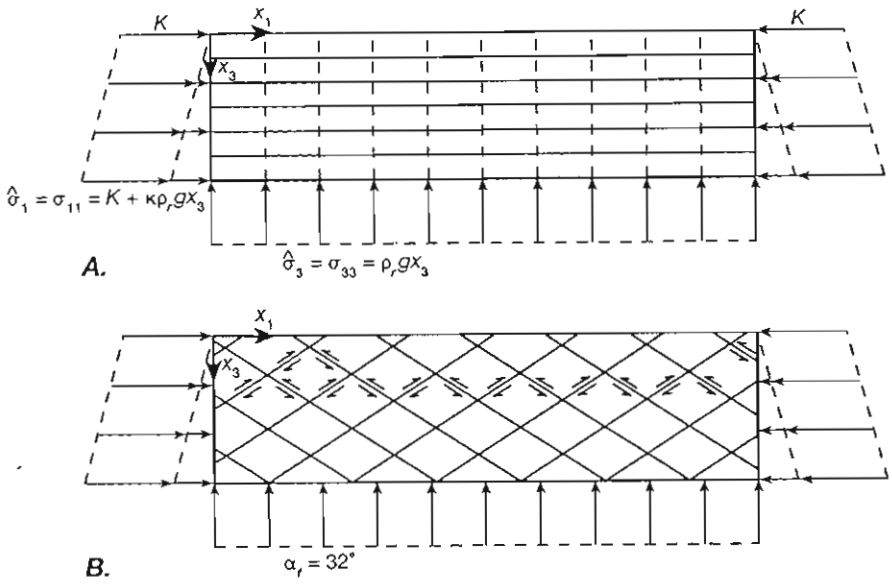

Figure 10.14 Free-body diagram for a horizontal compressive tectonic stress (K) constant with depth added to the standard state stress, which consists of a horizontal stress that increases with depth, and the vertical overburden. *A*. Tractions and stress trajectories. Solid lines are trajectories of $\hat{\sigma}_3$. *B*. Attitudes of potential shear fractures, assuming a fracture plane angle $\alpha_f = 32°$.

ficiently large, the horizontal stress becomes the maximum compressive stress $\hat{\sigma}_1 = \sigma_{11}$, as shown in Figure 10.14*A*. The potential faults, shown in Figure 10.14*B*, are a conjugate set of thrust faults, and the geometry corresponds to that assumed in Anderson's theory.

This model of the stress distribution is unrealistically simple. In particular, we have assumed that no shear stresses exist on the boundaries of the crustal block. As a result, all the stress trajectories are straight lines. If a crustal block were extending or shortening, for example, we would expect shear stresses opposing the motion to be present along the base of the block.

Consider the effect, therefore, of adding a horizontal shear stress that increases with depth and has a constant magnitude along the base of the block (Figure 10.15*A*).

$$\sigma_{31} = kx_3 \qquad (10.4)$$

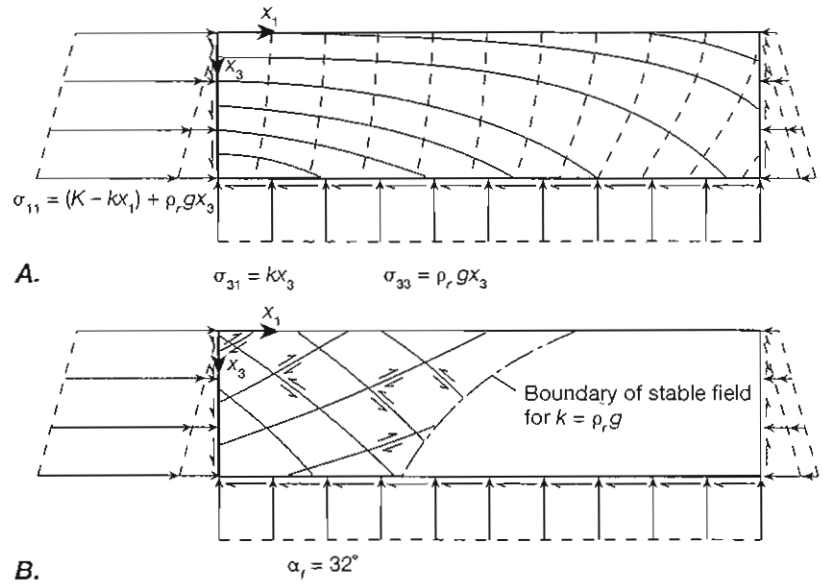

Figure 10.15 Free-body diagram for a compressive tectonic stress added to the standard state stress and including shear stresses on the boundaries of the block. *A*. Tractions and stress trajectories. Solid lines are trajectories of $\hat{\sigma}_1$; dashed lines are trajectories of $\hat{\sigma}_3$. *B*. Potential fault surfaces. The blank area indicates the region of stability where stresses are subcritical, as determined by the fracture criterion given in terms of the principal stresses by $\hat{\sigma}_1 = 4\hat{\sigma}_3 + 100$[MPa], where $\rho_r g = 25$ MPa/km and the value of $k = \rho_r g$ is chosen as an example.

This assumption also is overly simple, but the results are interesting. The symmetry of the stress tensor requires that vertical shear stresses balance the horizontal ones. Shear stresses must exist on the vertical boundaries of the block. Moreover, the requirement that all horizontal forces must sum to zero means that the horizontal normal force on the right side of the block must be less than that on the left, the difference being made up by the force contributed by the sheat stress on the base.

The fact that shear stresses exist on the sides and bottom of the block means that these boundaries are no longer principal planes of stress and that the principal axes in general are no longer horizontal and vertical. The top of the block, however, still supports no shear stress, so it must be a principal plane, and the vertical

boundaries just at the free surface must also be principal planes. Thus the shear stress on both horizontal and vertical planes must diminish to zero at the surface, as indicated by Equarion (10.4). The principal stress trajectories, thetefore, are horizontal and vertical at the surface and curve with depth to provide the shear stress on the vertical and horizontal surfaces that increases with depth (Figure 10.15*A*). With this stress distribution, the porential fault surfaces (Figure 10.15*B*) show a curvature comparable to that found on natural faults (compare Figure 6.12). Two possible directions of faulting are shown; one concave upward, reminiscent of many listric thrust faults, and one concave downward, reminiscent of faults along some basement uplifts (compare Figure 6.9).

Other possible boundary conditions, consisting of different stress distributions applied to the boundaries of the block, can of course be considered, and they lead to models of different tectonic environments. The diagram in Figure 10.16, for example, shows a stress distribution along the base of the block consisting of a sinusoidally varying vertical normal stress as well as a cosinusoidally varying horizontal shear stress. The standard state of stress is not shown in the diagram but is assumed to be added to the stress shown. The imposed stresses cause a bending of the block, and the stress trajectories are comparable to those in the folded layer in Figure 10.12C. This stress distribution is a possible model for a midoceanic spreading center where upwelling and laterally spreading material provide a vertical tectonic stress that decreases laterally from the spreading axis. The potential fault surfaces form a conjugate set of normal faults symmetrically oriented about the center of the block. Listric normal faults dip toward the center on both sides, and the conjugate faults dip away from the center and steepen with depth. The listric faults are comparable to faults observed on either side of the spreading axis of midoceanic ridges (compare also with the distribution of fractures on folds: Figures 3.17*E* and 10.12C and Table 10.1).

10.10 Determination of the Stress Field from Faults

The relationship between faults and principal stress directions implied by the Coulomb fracture criterion (Figures 9.4*B, D, E,* and 9.5*A*) suggests that we can use faults to estimate the orientation of the principal stresses. The reliability of such estimates depends on the nature of the faulting and the preservation of features indicating movement along them. For two sets of faults to be firmly identified as conjugate faults, the angle between them should be between about 40° and 90°, they must have opposite senses of shear, and there must be good evidence—such as mutual cross-cutting—that the two fault orientations were active at the same time. In such cases, we assume that the line of intersection of the conjugate faults is the intermediate principal stress direction ($\hat{\sigma}_2$), that the maximum compressive stress direction ($\hat{\sigma}_1$) bisects the acute angle between the fault planes, and that the minimum compressive stress ($\hat{\sigma}_3$) bisects the obtuse angle (Figure 10.10).

Shear fractures can develop, and shearing can occur, however, on preexisting fractures, faults, bedding planes, or other planes of weakness that are not in the orientation predicted by Coulomb theory. Moreover, the shear fractures predicted by Coulomb theory can accommodate extension or shortening only in the $\hat{\sigma}_1$–$\hat{\sigma}_3$ plane. If there is a component of extension or shortening parallel to $\hat{\sigma}_2$, the Coulomb criterion cannot predict the orientation of the fractures that form.

Fractures associated with a major fault commonly have a wide variety of orientations on which slickenside lineations, or slickenlines, are developed. Such lineations are parallel to the direction of slip on the different shear planes. If we assume the slip directions are parallel to the direction of maximum resolved shear stress on each plane, we can calculate the orientation of slickenline that should develop on any given plane whose orientation relative to the principal stresses, is known. We

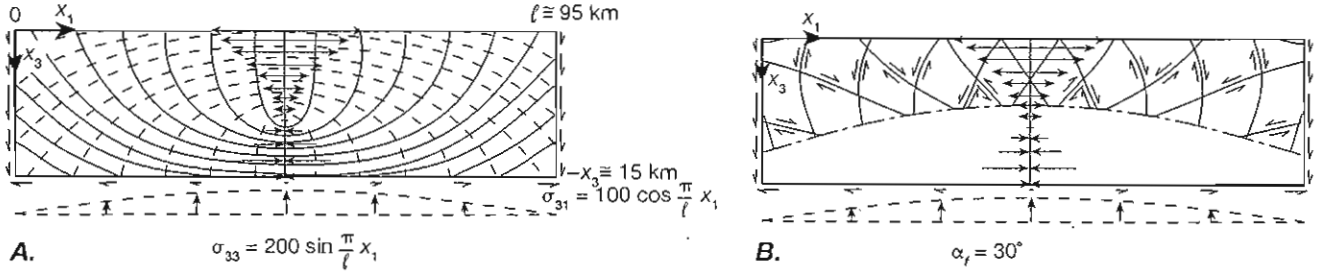

Figure 10.16 Free-body diagram for a block, with the normal stress on the base varying as a sine function, and shear stress on the base varying as a cosine function. The standard state is not shown but is assumed to be part of the stress stare. *A.* Tractions and stress trajectories. Solid lines are trajectories of $\hat{\sigma}_1$; dashed lines are trajectories of $\hat{\sigma}_3$. *B.* Potential fault surfaces. The blank area shows the field of stability if the maximum value of σ_{33} is 200 MPa.

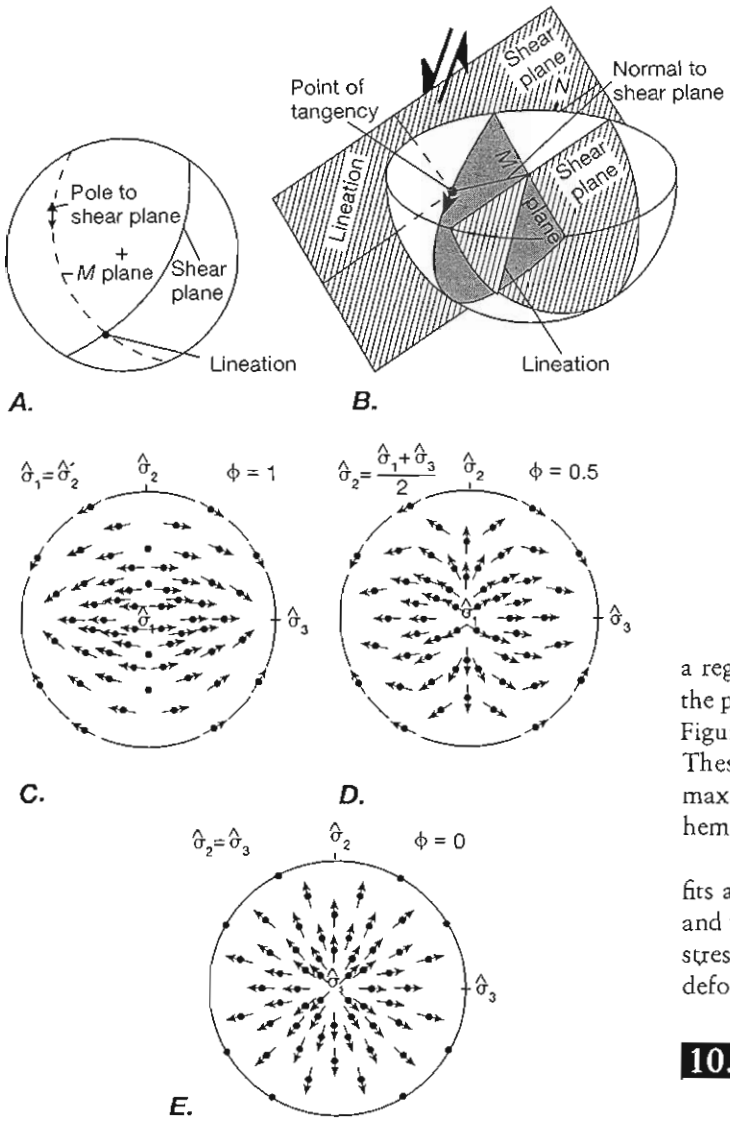

Figure 10.17 Construction and interpretation of tangent-lineation diagrams for slickenside lineations. *A.* The tangent lineations are plotted as arrows through the pole to the shear plane, tangent to the great circle that contains the shear plane pole and the lineation orientation in the shear plane. The arrow points in the direction of shear of the footwall. *B.* Interpretation of the tangent-lineation diagram. The shear plane is tangent to the outside of the plotting hemisphere at the shear plane pole. The arrow is parallel to the slickenline in the shear plane and indicates the shear sense of the footwall block on the shear plane. Note that both equal-area and equal-angle projections distort the true trend of the slickenline. *C, D, E.* Directions of maximum resolved shear stress on a set of planes having a uniform distribution of orientations over the plotting hemisphere for different values of the stress difference ratio ϕ. $\hat{\sigma}_1$ is vertical, $\hat{\sigma}_2$ is horizontal at the top and bottom of the stereogram, and $\hat{\sigma}_3$ is horizontal at the right and left sides of the stereogram. Lower-hemisphere, equal-angle projection.

plot these directions on a tangent-lineation diagram, which combines information about the shear plane orienration, the orientation of the slickenline in that plane, and the sense of shear on the plane.

To plot slickenline data on a tangent-lineation diagram (Figure 10.17*A*), we construct on a lower hemisphere projection the great circle that contains both the pole (the normal) to the shear plane and the orientation of the lineation in the shear plane, and we draw an arrow tangent to this great circle at the shear plane pole. The arrow points in the direction of relative shear of the footwall block. The pole to the shear plane is the point on the plotting hemisphere where the shear plane would be *tangent* to the *outside* of the hemisphere (Figure 10.17*B*). The arrow is then parallel to the slickenline in the tangent plane and points in the direction of relative shear of the footwall block for that plane. The directions of maximum resolved shear stress on a set of planes uniformly distributed on the plotting hemisphere form a regular pattern whose details depend on the ratio of the principal stress differences $\phi = (\hat{\sigma}_2 - \hat{\sigma}_3)/(\hat{\sigma}_1 - \hat{\sigma}_3)$. Figure 10.17*C–E* shows examples of such patterns. These diagrams therefore show the orientations of the maximum shear traction over the outside of the plotting hemisphere.

Using a computer, we can find the pattern that best fits a given set of field data on slickenline orientations, and we can thereby infer the orientation of the principal stresses and the stress difference ratio ϕ that caused the deformation.[4]

10.11 The Mechanics of Large Overthrusts

In Chapter 6 we discussed the existence of large overthrust sheets that extend for distances of up to hundreds of kilometers along strike and over 100 km across strike. Such large thrusts have been known since the end of the nineteenth century. Soon after they were recognized, however, it became clear that to push such a large mass would seem to require forces that the rocks would be unable to withstand.

M. S. Smoluchowski first formulated the problem in elemetary form in 1909. Consider a rectangular block of height H (parallel to coordinate axis x_3), width W parallel to the thrusting direction (and to coordinate

[4] A more general theory of slickenline orientations is obtained by assuming they are parallel to the direction of maximum rate of shear on any particular surface and by accounting specifically for the rotation of the shear planes. The patterns shown in Figure 10.17*C–E* emerge for a special case.

x_1), and length L perpendicular to the direction of motion (and parallel to coordinate x_2). Its weight per unit volume is $\rho_r g$, and the coefficient of sliding friction on the block's base is $\bar{\mu}$. The frictional force that resisrs the motion of the block (F_f) equals the normal force across the base (F_n) times the coefficient of friction ($\bar{\mu}$). That is,

$$F_f = \bar{\mu} F_n \tag{10.5}$$

$$= \bar{\mu} \times (\text{normal force per unit area}) \times (\text{area})$$

$$F_f = \bar{\mu}(\rho_r g H)(WL) \tag{10.6}$$

The driving force required to move the block must be greater than or equal to the frictional resistance. If the driving force is applied across the back vertical face of rhe block, the stress on that face is the driving force per unit area,

$$\sigma_{11} = \frac{F_f}{LH} = \bar{\mu}\rho_r g W \tag{10.7}$$

where we inttoduced Equation (10.6) for F_f. This stress cannot exceed the fracture strength of the block. Choosing average values for the coefficients of friction, density, and strength ($\bar{\mu} = 0.6$, $\rho_r = 2500$ kg/m^3, and $\sigma_{11}^* = 250$ MPa), we can solve Equation (10.7) for W.

$$W = \frac{\sigma_{11}^*}{\bar{\mu}\rho_r g} = 17{,}007 \text{ m} = 17 \text{ km} \tag{10.8}$$

Thus this model predicts that the maximum possible dimension of an overthrust sheet in the direction of thrusting is $W = 17$ km. For larger dimensions, the fracture strength of the rock is exceeded at the rear face of the sheet before the frictional resistance can be overcome. Large overthrusts, however, are known to have widths W of over 100 km, so something must be wrong with this model. A more sophisticated analysis yielding more general but comparable results is given in Box 10.2.

There are several assumptions in this simple model that may be inappropriate for explaining the mechanics of emplacement of large thrust sheets: (1) The force of friction on the base of the thrust could be lowcr than we assumed. (2) The very assumption that resistance to motion is frictional in origin may be incorrect, and the shear along the décollement in some cases may be accommodated by ductile flow of weak rocks. (3) The thrust sheet may be driven not by a push from the rear but by gravitational forces. (4) Thrust sheets in general are not rectangular blocks, as assumed in our model, but instead taper to smaller thicknesses toward the foreland. (5) Thrust sheets do not move en masse as a single sheet, but rather caterpillar style, by the propagation of localized domains of slip along the fault. All of these factors may be important in explaining aspects of the mechanics of thrust sheets.

Basal Friction

The force of frictional resistance can be reduced in two possible ways: The coefficient of friction $\bar{\mu}$ on the base can be significantly smaller than we assumed, either intrinsically or because of lubrication, or the effecrive normal stress across the décollement can be less than we assumed.

Laboratory measurements of the coefficient of friction of rock on rock consistently give values near $\bar{\mu} = 0.85$ and do not leave much possibility for significant reduction. The presence of water on a rock interface actually seems to increase the coefficient of friction; it does not act as a lubricant.

A high pore fluid pressure along the décollement, with λ approaching 1, would reduce the effective normal stress across the surface and thereby lower the frictional resistance (Equation 10.5; see Section 9.5). If the frictional resistance decreases, then a horizontal normal stress that is equal to the critical fracture srress can move a greater width of thrusr sheet. For zero resistance, the possible width of the thrust sheet is unlimited. Sedimentary basins in active tectonic regions are prime locations for the formation of high pore fluid pressure (Section 10.3), and large overthrust sheets are common in such environments. This explanation has been accepted as a fundamental mechanism associated with the emplacement of large thrust sheets, but it is not a complete explanation.

Ductile Flow

Thrust faults commonly follow layers of weak rock in the stratigraphic section. Evaporites, and especially halite (common rock salt), are among the weakest rocks known. For conditions characteristic of geologic deformation, halite has a yield stress in the range of 0.1 to 1 MPa. Even at shallow depths and low temperatures, the differential stress that makes halite flow is one to two orders of magnitude less than frictional stresses and the yield stresses of other rocks.

Large accumulations of evapotites (such as halite, gypsum, and anhydrite) underlie many sedimentary basins, including the Gulf Coast of the United States, southwestern Iran, and the Appalachian plateau in western Pennsylvania and adjacent states. The resistance to the motion of thrust sheets can therefore be determined by the yield stress of halite rather than the considerably higher frictional stresses. The yield stress, moreover, is relatively insensitive to pressure, unlike friction. Thus where thrust faults can occupy salt beds, the resistance to motion is significantly less than where the salt is absent, and our model would suggest that in those areas, the thrust sheets can extend much farther out toward the foreland. This explanation accounts for the major

Box 10.2 Simple Model of a Thrust Sheet

We adopt a model of a thrust sheet composed of cohesionless material underlain by a horizontal décollement on which motion occurs by frictional sliding. In general, the height of the sheet as a function of the horizontal distance in the direction of displacement x_1 is $h(x_1)$, and for the maximum dimensions of the sheet, when $x_1 = W$, then $h(W) = H$ (Figure 10.2.1). The tractions acting on the external surfaces of the thrust sheet are as shown in Figure 10.2.1, and they include a horizontal tectonic traction σ_t^+ applied to the rear vertical face of the sheet, a vertical traction $\sigma\bar{v}$ applied along the bottom of the thrust sheet, and a frictional shear traction σ_f^- also applied along the bottom of the thrust sheet. The superscript + and − indicate that we are considering the traction components acting on the positive and negative sides of the coordinate planes, respectively.

The sum of the horizontal tectonic force F_T and the total force of frictional resistance on the base F_F must be zero if the thrust wedge is moving as a block but not accelerating.

$$F_T + F_F = 0 \qquad (10.2.1)$$

where

$$F_T = \int_0^H \sigma_t^+ \, dx_3, \quad \text{at } x_1 = W \qquad (10.2.2)$$

$$F_F = \int_0^W \sigma\bar{F} \, dx_1, \quad \text{at } x_3 = 0 \qquad (10.2.3)$$

The frictional traction $\sigma\bar{f}$ is related to the effective vertical traction $(\sigma\bar{v} - p_f)$ by the coefficient of friction on the base $\bar{\mu}_b$.

$$\sigma\bar{F} = \bar{\mu}_b[\sigma\bar{v} - p_f^{(b)}], \quad \text{at } x_3 = 0 \qquad (10.2.4)$$

where $p_f^{(b)}$ is the pore fluid pressure on the base of the sheet.

We now make the following assumptions: (1) The horizontal stress is approximately the maximum compressive stress. (2) The horizontal stress is as large as possible and thus is given by the Coulomb fracture criterion. (3) The vertical stress is approximately the minimum compressive stress and equals the overburden pressure. We express assumption 2, the Coulomb fracture criterion, in terms of the principal stresses by using Equation (9.1.2) with the effective principal stresses ${}_E\hat{\sigma}_k = \hat{\sigma}_k - p_f^{(i)}$ substituted for the principal stresses. Thus

$$\hat{\sigma}_1^* - p_f^{(i)} = S + K(\hat{\sigma}_3 - p_f^{(i)})$$

where $p_f^{(i)}$ represents the internal pore fluid pressure of the wedge. Setting $S = 0$ to represent the fracture criterion for a cohesionless material, and rearranging the equation, we find that

$$-\sigma_t^+ = \hat{\sigma}_1^* = K\hat{\sigma}_3 - (K-1)p_f^{(i)}, \quad \text{at } x_1 = W \qquad (10.2.5)$$

where the minus sign is introduced because the traction σ_t^+ has the opposite sign from the stress component. (It acts on the positive side of the coordinate surface, and we use the geologic sign convention, which assigns the stress component the sign of the traction acting on the negative side of the surface.) We express assumption 3 as

$$\sigma\bar{v} = \hat{\sigma}_3 = \rho_r g(h - x_3) \qquad (10.2.6)$$

These assumptions imply that the principal stresses are everywhere horizontal and vertical, which cannot actually be true because there is a shear stress on the horizontal base of the sheet. Thus the stress trajectories should be inclined, but our simplifying assumption should be a reasonable first approximation if the shear stress is relatively small and therefore the inclination of the maximum principal stress is small.

In order for sliding to occur on the base, rather than faulting to occur within the wedge, the coefficient of sliding friction on the base must be less than the coefficient of internal friction for the Coulomb fracture criterion; that is, $\bar{\mu}_b < \mu_i$. The pore fluid pressures internal to the wedge and along the base can be expressed as a fraction λ of the vertical stress:

$$p_f^{(i)} = \lambda_i \rho_r g(h - x_3) \qquad p_f^{(b)} = \lambda_b \rho_r g h \qquad (10.2.7)$$

where i and b as superscripts or subscripts indicate the variable *internal* to the wedge or along the *base*, respectively, and where in the second equation x_3 does not appear because it is zero along the horizontal décollement. We assume that λ_b is constant along the décollement and that λ_i is constant within the thrust wedge.

We now combine Equations (10.2.1) through (10.2.7) to obtain

$$[K - (K-1)\lambda_i] \int_0^H (H - x_3)\, dx_3 = \bar{\mu}_b(1 - \lambda_b) \int_0^W h \, dx_1 \qquad (10.2.8)$$

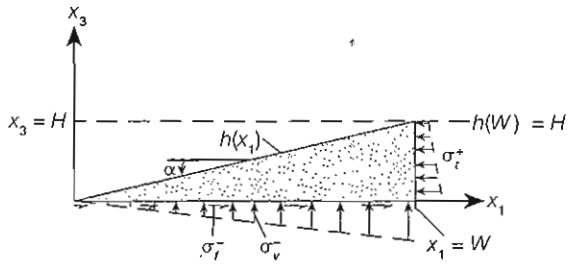

Figure 10.2.1 Model for a thrust sheet, showing the geometry and the tractions acting on the surfaces.

Integrating the left side of the equation, which is the tectonic traction across the height of the rear face of the thrust wedge (where $x_1 = W$ and $h = H$) and collecting constants on the left side of the equation, we find that Equation (10.2.8) becomes

$$0.5\ CH^2 = \int_0^W h\ dx_1 \qquad (10.2.9)$$

where

$$C = \frac{K - (K-1)\lambda_i}{\bar{\mu}_b(1-\lambda_b)} = \frac{(K-1)(1-\lambda_i)+1}{\bar{\mu}_b(1-\lambda_b)} \qquad (10.2.10)$$

Note that if there is no pore fluid pressure, then λ_i and λ_b are both zero, and C is the ratio of the fracture strength constant of the thrust sheet, K, to the frictional resistance on the base, $\bar{\mu}_b$. In general, then, C is just this ratio modified by the effects of pore fluid pressure. Equation (10.2.9) can be interpreted in two different ways, which we discuss in turn below.

We can assume that the thrust sheet must be everywhere below the critical Coulomb fracture stress, and we assume a particular shape $h(x_1)$ for the thrust sheet. With H a given constant, we can interpret Equation (10.2.9) as determining the limiting cross-sectional width of the thrust sheet W for which the stress in the thrust sheet remains below the critical value. Supposing the thrust sheet to be a rectangular block, we choose $h(x_1)$ to be a constant H for the whole thrust sheet. We considered this problem in a simplified way at the beginning of Section 10.11. Upon integrating the right side of Equation (10.2.9) and rearranging, we find that

$$W = 0.5CH \qquad (10.2.11)$$

Thus for a given thickness H of a block-shaped thrust sheet, and for given values of K, $\bar{\mu}_b$, λ_i, and λ_b, which determine C, this relationship gives the maximum width W for a thrust sheet that can be moved over the décollement. We assume for simplicity that $\bar{\mu}_b = \mu_i$ and that $\lambda_b = \lambda_i$, and we use Equation 10.2.10 and the values from Table 10.2.1 to graph the dependence of $C/2 (= W/H)$ on λ (Figure 10.2.2A). For zero pore fluid pressure, $C/2$ is between 2.75 (for $\theta_f = 65°$) and 3.85 (for $\theta_f = 50°$). Thus for a thrust

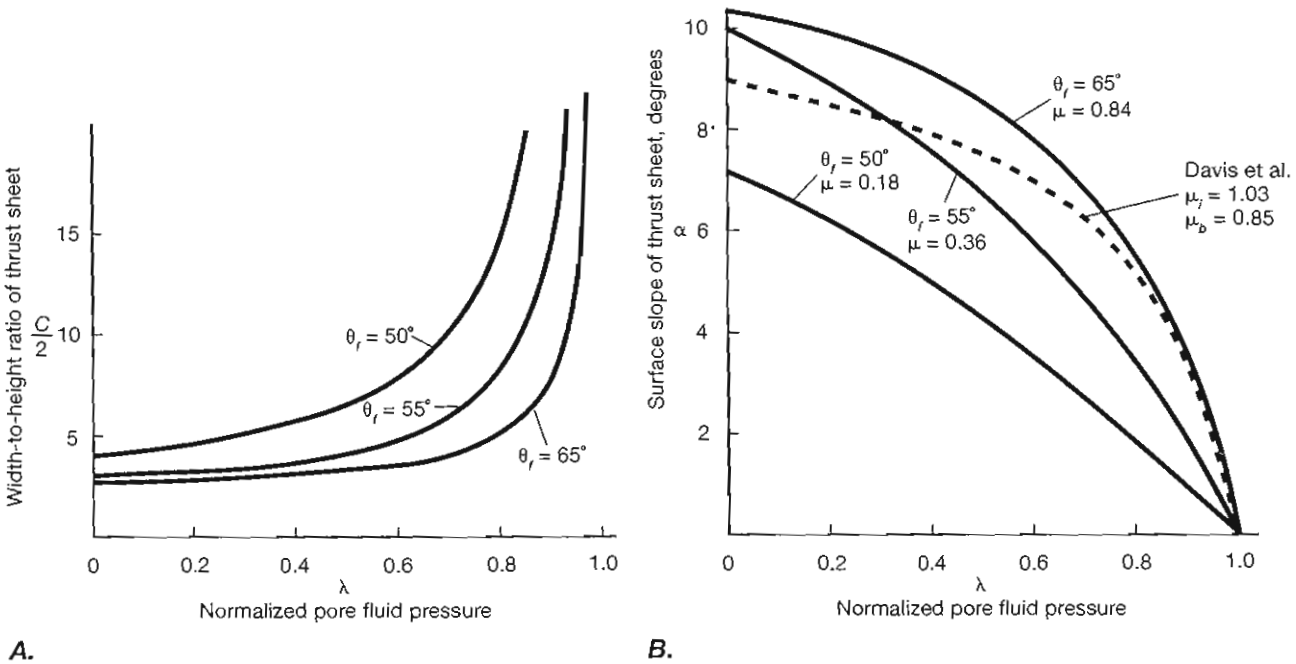

Figure 10.2.2 Permissible geometry of thrust sheets as a function of the pore fluid pressure ratio λ. *A*. Maximum possible ratio of width to height ($C = 2W/H$) for a thrust sheet shaped like a rectangular block, plotted as a function of λ. *B*. Equilibrium surface slope α for a wedge-shaped thrust sheet with a horizontal décollement, plotted as a function of λ. Solid lines result from the present analysis; the dashed line results from the more detailed model of Davis et al., 1983.

Box 10.2 *(continued)*

sheet of thickness $H = 5$ km, the width W must be between about 13.7 km and 19.7 km, for the different values of the fracture angle θ_f. This result is of the same order as the more approximate solution in Equation (10.8). Note that the possible length of the thrust sheet increases without limit as λ approaches 1.

For an alternative interpretation of Equation (10.2.9), we can assume that the entire thrust sheet must be just at the critical Coulomb fracture stress, and we take H and W to be variables. Equation (10.2.9) then defines the shape of the thrust sheet, because it prescribes how the height H must vary with the cross-sectional length W across the thrust sheet in order that the thrust sheet be everywhere at the critical Coulomb stress. Equation (10.2.9) can be satisfied only if $h(x_1)$ is a linear function of x_1, because the integral must have dimensions of [length]^2.

$$h(x_1) = Ax_1 + B \tag{10.2.12}$$

We require that

$$h(W) = H \qquad A = \tan \alpha \tag{10.2.13}$$

where the first Equation (10.2.13) is implicit in the way the quantities are defined for the problem, and where α is defined as the surface slope of the wedge. Substituting this equation into Equation (10.2.12) shows that

$$H = AW + B \tag{10.2.14}$$

$$\int_0^W h\, dx_1 = \int_0^W (Ax_1 + B)\, dx_1 = 0.5AW^2 + BW \tag{10.2.15}$$

Substituting Equations (10.2.14) and (10.2.15) into Equation (10.2.9) and simplifying, we get

$$0.5[A^2C - A]W^2 + [ABC - B]W + 0.5[B^2C] = 0 \tag{10.2.16}$$

This relationship must hold for a thrust wedge of any width W, and for this to be true, each of the coefficients in brackets must independently be zero:

$$A^2C - A = 0 \qquad ABC - B = 0 \qquad B^2C = 0 \tag{10.2.17}$$

To satisfy the third Equation (10.2.17), either $B = 0$ or $C = 0$. Taking $C = 0$ implies from Equation (10.2.10) that K is a function of λ_i or, through the second Equation (9.1.3) that the fracture angle θ_f is a function of the pore pressure ratio. Experimental work shows that this is a physically unacceptable solution, so we must choose $B = 0$. This result implies, from Equation (10.2.12), that the thrust wedge tapers to a point, which is physically reasonable for a material with no cohesion (Figure 10.2.1).

Both the first and second Equations (10.2.17) give exactly the same condition,

$$A = \frac{1}{C} \tag{10.2.18}$$

Introducing Equation (10.2.10) and the second Equation (10.2.13) into Equation (10.2.18), we find that

$$\tan \alpha = \frac{\bar{\mu}_b(1 - \lambda_b)}{(K - 1)(1 - \lambda_i) + 1} = \frac{1}{C} \tag{10.2.19}$$

where α is the topographic slope angle of the thrust wedge.

If $\lambda_b = \lambda_i = 0$—that is, if there is no pore fluid pressure—the surface slope of the thrust wedge is determined by $\bar{\mu}_b/K$, the ratio of frictional resistance on the base of the sheet to the fracture strength constant of the thrust wedge. As the pore fluid pressure internal to the wedge increases, the effect is to decrease the strength of the wedge. Thus for higher values of λ_i, the denominator of Equation (10.2.19) decreases, the ratio increases, and the surface slope of the thrust wedge increases. As the pore fluid pressure along the base increases, there is less resistance to frictional sliding. Thus for higher values of λ_b, the numerator in Equation (10.2.19) decreases, the ratio decreases, and the surface slope of the thrust wedge decreases.

For purposes of simplification, we assume $\mu_i = \bar{\mu}_b = \mu$ and $\lambda_i = \lambda_b = \lambda$. Figure 10.2.2*B* shows the relationships then predicted by Equation (10.2.19) between the topographic slope α of the thrust sheet and the magnitude of the pore fluid pressure ratio λ for values of the constants in Table 10.2.1. The predicted slopes are all less than about 10°. The slopes approach 0°, and the frictional resistance to sliding on the décollement decreases toward zero as λ approaches 1. These results are comparable to the angles calculated from more sophisticated analyses for the same angle of the décollement (Figure 10.2.2). More thorough analyses include the dip of the décollement as a variable.

Table 10.2.1 Relationships Among Fracture Angle, Coefficient of Internal Friction, and K[a]

θ_f	μ_i	K
65	0.84	4.60
60	0.58	3.00
55	0.36	2.04
50	0.18	1.42
45	0.00	1.00

[a] Given θ_f, the tabulated values of μ_i and K are calculated from Equations (9.1.1) and (9.1.3).

salient in the northwestern Appalachians (Figure 6.11*A*). Here the large belt of very gentle folding in the Appalachian plateau northwest of the Valley and Ridge province is almost coincident with the extent of Silurian salt beds at depth.

Anhydrite and gypsum also have relatively low yield stresses, and strata rich in these minerals also commonly act as décollement zones. Where evaporites are not present, shales are generally the weakest rocks, and at greater depths and higher temperatures, limestone (marble) and even quartzite may be sufficiently weak to localize major zones of ductile shear in a décollement.

Gravitational Driving Forces

One problem with our simple model arises from the need to drive the thrust sheet forward by means of a stress transmitted through the thrust sheet from the rear. If the force of gravity were the driving force, however, this restriction would not arise, because gravitational forces act independently on every point in a body.

Gravitational sliding occurs if the shear force provided by the force of gravity (F_s) is at least equal to the frictional resistance on the décollement ($F_s = F_f$; Figure 10.18*A*). If we know the resistance, we can determine the slope necessary to cause such a thrust sheet to slide. From Equation (10.5), therefore, we have

$$\bar{\mu} = F_s/F_n \tag{10.9}$$

If gravity is the only force driving the sheet, then the normal force across the décollement (F_n) and the shear force parallel to it (F_s) are related to the dip δ of the thrust surface by

$$\tan \delta = F_s/F_n$$

Using Equation (10.9), and assuming that the coefficient of friction $\bar{\mu} = 0.6$, which is actually a low value compared with most experimental data, we find that

$$\tan \delta = \bar{\mu} \approx 0.6$$

$$\delta = 31°$$

Thus a slope of at least 31° is required to move the thrust block gravitationally against a conservative value of the frictional resistance. A 100-km thrust sheet would need to slide off a topographic high of at least 51.5 km altitude for this mechanism to explain some of the larger thrust sheets (Figure 10.18*B*). Given that Mt. Everest is less than 9 km above sea level, this solution does not appear to be satisfactory. Moreover, evidence for steep dips over significant lengths of large thrust sheets is utterly lacking. This mechanism could account for the observations only if it were effective on slopes on the order of a few degrees at most. Such slopes imply a very small resistance along the décollement, and we must therefore include in the model either high pore fluid pressure or ductile flow to make it acceptable.

If tectonic processes thicken the crust and create a topographic high, gravitational collapse of the thickened part of the crust could result in the formation of thrust sheets. This mechanism requires ductile flow throughout much of the thickened part of the crust, which spreads outward under its own weight rather like a mound of silicon putty spreads out into a puddle, or, to draw an even more apt analogy, like a continental ice sheet spreads out from its center (Figure 10.18*C*). The driving force is provided by the topographic slope of the thickened region of crust, and the slope of the décollement is not restricted; it could even slope upward in the direction of thrusting, as is a common feature of thrust sheets.

Intuitively, gravitational forces may not seem strong enough to cause rocks to deform significantly. We must not forget, however, that ultimately, gravitational forces drive the whole plate tectonic machine

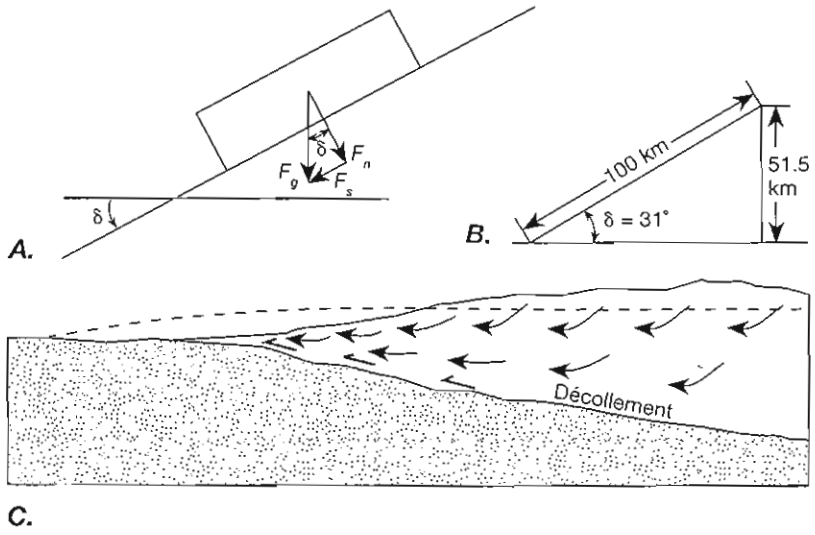

Figure 10.18 Models of gravitationally driven thrust sheets. *A*. Resolution of the gravitational force on a thrust sheet to determine the driving force available (F_s) and the normal force across the décollement (F_n). *B*. Normal rock friction would require too steep a slope to account for the size of thrust sheets and dips of décollement observed. *C*. Gravitational collapse of a tectonically produced topographic high by ductile flow within the thrust sheet. The solid lines indicate the tectonically uplifted topography; the dashed line indicates the topography after gravitational collapse of the uplift. Arrows indicate the general pattern of flow within the collapsing sheet.

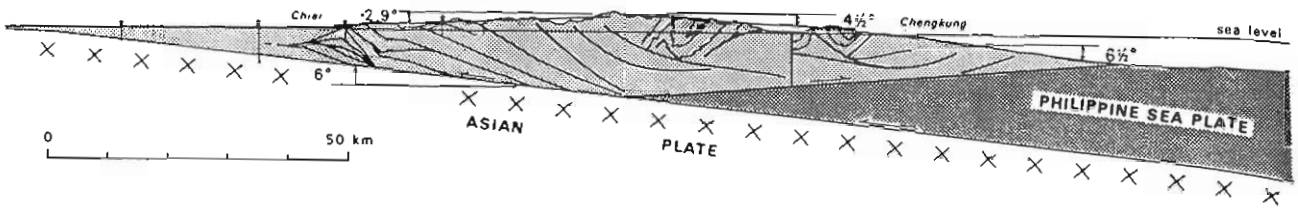

through mantle convection. Given the great lengths of time available, and the ability of rocks to creep slowly in response to relatively small differential stresses, emplacement of thrust sheets by gravitational collapse cannot be discounted.

Tapered Thrust Sheets

Active thrust sheets, such as occur in western Taiwan and in the Himalayas, and active submarine aecretionary prisms over subduction zones are wedge-shaped, rather than rectangular, in cross section, with thickness increasing with increasing distance from the front of the thrust sheet (Figure 10.19). We can account for this tapered shape by means of a simple model. We assume that the rocks in the thrust sheet are everywhere just at the critical stress for failure. Furthermore, we require that the driving force on a vertical face through the sheet just balances the frictional resistance to sliding on that part of the décollement that lies ahead of the vertical face. The force resisting sliding on the décollement must increase with increasing distance from the front of the thrust sheet. Thus the driving force on a vertical face must also increase with increasing distance from the front. Because the driving *stress* is limited by the strength of the rock, the driving *force* can increase only if the area of the vertieal face increases, and this means the thickness of the thrust sheet must increase. Thus the thickness of the thrust sheet at any point depends on the length of the sheet ahead of that point that must be moved, resulting in a thrust sheet that has a wedge shape (see Box 10.2).

The determination of a proper mechanical model for sueh a thrust wedge is complex (see Box 10.2). The surface slope of the wedge actually is affected not only by the resistance to motion of the décollement but also by the slope of the décollement. Moreover, resistance to sliding can be affected by the pore fluid pressure or by the presence of weak ductile rock along the décollement. This simple analysis of the driving force also ignores the small horizontal pressure gradient created by the surface slope of the thrust sheet. The mechanics of such wedges, however, is similar to the mechanics of dirt and snow wedges that would form in front of bulldozer and snowplow blades if the blades were flat

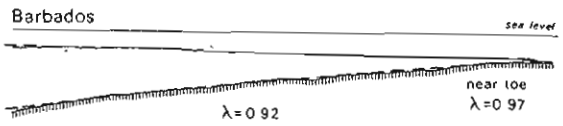

Figure 10.19 The rapered wedge model of thrust sheers is supporred by observations of the geometry of acrive continental fold-and-thrust belts such as in western Taiwan and by submarine accretionary prisms that overlie acrive subduction zones such as easr of Barbados in the eastern Carribbean Sea.

and vertical.[5] Such a wedge is the thinnest body of a given width parallel to the direction of thrusting that can be slid over the décollement.

If material is added to the front, or toe, of the wedge, the whole wedge deforms ro maintain the critical tapet. The deformation takes the form of thrust faults, folds, and fault ramp folds intetnal to the wedge, all of which result in a net shortening and thickening of the wedge (Figure 6.12). If the taper of the wedge becomes too large, then the thrust fault propagates out in front of the wedge to lengthen the thrust sheet and dectease the taper; internal faulting and folding provide the adjustments to the taper throughout the rest of the sheet.

A comparison of the tapered wedge model with observations is indicated in Figure 10.20, which plots the dip of the décollement β against the dip of the surface slope α. The lines are the theoretically predicted relationship for a variety of values for the pore fluid pressure ratio λ. The boxes indicate the approximate geometries of active wedges as labeled. It is clear from this figure that most thrust wedges require a value of λ considerably above the hydrostatic value of about 0.4, implying significant overpressure of the pore fluid. Such values of λ are consistent with measurements made in wells that penetrate into some of these wedges, which lends credence to the theory. The presence of salt along the

[5] In fact, however, such plow blades are vertically curved, a design that forces the snow or dirt to slide up the blade and fall forward, creating a pile whose taper is the angle of repose of the marerial rather than the critical taper under discussion here. The angle of repose is thc angle of steepest slopc that loose material can support, and it is generally about 30°, whereas the steepest slopes predicted by the tapered thrust sheet model are about 10°. Thus this analogy can be somewhat misleading.

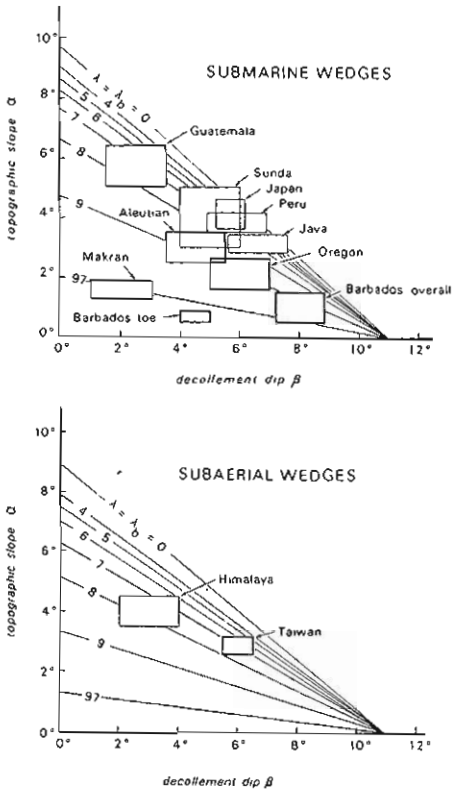

Figure 10.20 The measured geometry of subaerial and submarine thrust wedges compared with the theoretically predicted relationships among the topographic slope angle α, the slope of the décollement β, and the pore fluid pressure ratio λ.

décollement, however, could result in surface slopes as low as 1° and thus could also account for some of the very low slopes observed.

The Propagation of Slip Domains

The foregoing discussion of the mechanics of a thrust sheet assumes the entire mass is at the critical stress for fracture that is predicted by the Coulomb fracture criterion. This is a simplifying assumption, however, because the entire thrust sheet does not move as a rigid block or undergo pervasive deformation at one time. Rather, the deformation is accommodated by the propagation of discontinuous slip events over finite areas of faults within and at the base of the sheet. Such slip events, which are localized in time and space, commonly cause earthquakes that we can observe. Only by averaging these evenrs over a long period of time — perhaps tens to hundreds of thousands of years — would we see the pattern of pervasive deformation and the slip of the entire thrust sheet on the décollement that we assume for the model. The applied stress needed to make slip events propagate across the fault is lower than that required to make the entire thrust fault slip at once, an effect that should be accounted for in mechanical models of faulting. The effect is similar to the propagation of dislocations in a crystal lattice, which we discuss in Chapter 19.

10.12 Cause and Effect: A Word of Caution

Our interpretations in this chapter of the origin of brittle deformation structures, including application of the fracture criteria that we discussed in Chapter 9, implicitly assume that stress is the cause of the deformation. Although this is often a very useful assumption, it is not necessarily appropriate in all situations.

The cause of a mechanical process essentially is determined by the boundary conditions, which are the conditions that are externally imposed both on the boundaries of a body and throughout it as distributed sources, such as the force of gravity. If stresses are imposed and maintained on the boundaries of the body, then stress is the cause of the process, and deformation develops in response to the imposed stress. If, however, the boundaries of the body are required to move a prescribed amount or at a prescribed rate in a prescribed direction—that is, the deformarion is prescribed on the boundaries of the body—then the deformation is the cause of the process, and the stresses develop in response to the imposed deformation. Under these circumstances, the origin of different structures is better understood with reference to the deformation.

We discuss strain, a measure of deformation, and its application to the interpretation of structures in Chapters 15 through 17; the relationships between stress and deformation are the ropic of Chapter 18; and the role of boundary conditions are discussed further in Section 20.1.

Additional Readings

Stress in the Plates

Brace, W. F., and D. L. Kohlstedt. Limits of lithospheric stress imposed by laboratory experiments. 1980. *J. Geophys. Research* 85: 6248–6252.

McGarr, A. 1980. Some constraints on the levels of shear stress in the crust from observations and theory. *J. Geophys. Research* 85: 6231–6238.

McGarr, A., and N. C. Gay. 1978. Stare of stress in the earth's crust. *Ann. Rev. Earth and Planet. Sci.* 6: 405–436.

Richardson, R. M., S. C. Solomon, and N. H. Sleep. 1979.

Tectonic stress in the plates. *Rev. Geophys. and Sp. Phys.* 17: 981–1019.

Zoback, M. D., H. Tsukahara, and S. Hickman. 1980. Stress measurement at depth in the vicinity of the San Andreas fault: Implications for rhe magnitude of shear stress at deprh. *J. Geophys. Research* 85: 6157–6173.

Zoback, M. L., and M. D. Zoback. 1980. State of stress in the coterminus United Stares. *J. Geophys. Research* 85: 6113–6156.

Zoback, M. L., er al. 1989. Global patrerns of tectonic stress. *Nature* 341: 291–298.

Formation and Interpretation of Joints

Bahat, D. 1979. Theoretical considerations on mechanical parameters of joint surfaces based on studies on ceramics. *Geol. Mag.* 116: 81–92.

Bahat, D. 1991. Plane stress and plane strain fracture in Eocene chalks around Beer Sheva. *Tectonophysics* 196: 61–67.

Bahat, D., and T. Engelder. 1984. Surface morphology on joints of the Appalachian plateau, New York and Pennsylvania. *Tectonophysics* 104: 299–313.

Brown, E. T., and E. Hoek. 1978. Trends in relationships berween measured *in-situ* srresses and deprh. *Int. J. Rock Mech. Mining Sci.. and Geomech. Abstr.* 15: 211–215.

Degraff, J. M., and A. Aydin. 1987. Surface morphology of columnar joints and irs significance to mechanics and direction of joint growrh. *Geol. Soc. Am. Bull.* 99: 605–617.

Engelder, T. 1985. Loading parhs to joint propagation during a tectonic cycle: An example from the Appalachian plateau, U.S.A. *J. Struct. Geol.* 7: 459–476.

Engelder, T., and P. Geiser. 1980. On the use of regional joint sets as rrajectories of paleostress fields during the development of the Appalachian plateau, New York. *J. Geophys. Research* 85: 6319–6341.

Haxby W. F., and D. L. Turcotte. 1976. Stresses induced by the addition or removal of overburden and associated thermal effecrs. *Geology* 4(3): 181–184.

Ladeira, F. L., and N. J. Price. 1981. Relationship between fracture spacing and bed thickness. *J. Struct. Geol.* 3(2): 179–184.

Kulander, B. R., and S. L. Dean. 1985. Hackle plume geometry and joint dynamics. In *Fundamentals of rock joints.* Proceedings of rhe International Symposium of Rock Joints, Bjorkliden, Sweden, 85–94.

Pollard, D. D., P. Seagall, and P. T. Delaney. 1982. Formation and interpretation of dilatant *en echelon* cracks. *Geol. Soc. Am. Bull.* 93: 1291–1303.

Fractures Associated with Faults

Beach, A. 1975. The geometry of *en-echelon* vein arrays. *Tectonophysics* 28: 245–263.

Conrad, R. E., II, and M. Friedman. 1976. Microscopic feather fractures in the faulting process, *Tectonophysics* 33: 187–198.

Engelder, T. 1974. Cataclasis and the generation of fault gouge. *Geol. Soc. Am. Bull.* 85: 1515–1522.

Friedman, M., and J. M. Logan. 1970. Microscopic feather fracrures. *Geol. Soc. Am. Bull.* 81: 3417–3420.

Fractures Associated with Folds

Cnrrie, J. B., H. W. Patnode, and R. P. Trump. 1962. Development of folds in sedimentary strata. *Geol. Soc. Am. Bull.* 73: 655–674.

Friedman, M., R. H. H. Hugman, III, and J. Handin. 1980. Experimental folding of rocks under confining pressure: Part VIII. Forced folding of unconsolidated sand and of lubricated layers of limestone and sandstone. *Geol. Soc. Am. Bull. Part I,* 91(5): 307–312.

Handin, J., M. Friedman, K. D. Min, and L. J. Partison. 1976. Experimental folding of rocks under confining pressure: Part II. Buckling of multilayered rock beams. *Geol. Soc. Am. Bull.* 87: 1035–1048.

Norris, D. K.. 1967. Structural analysis of the Queensway folds, Ottawa, Canada. *Canad. J. Earth Sci.* 4: 299–321.

Spang, J. H., and R. H. Groshong, Jr. 1981. Deformation mechanism and strain history of a minor fold from the Appalachian Valley and Ridge. *Tectonophysics* 72: 323–342.

Stearns, D. W. 1968. Certain aspects of fractures in naturally deformed rocks. In *NSF advanced science seminar in rock mechanics for college teachers of structural geology,* ed. R.E. Riecker, pp. 97–118. Bedford, Mass.: Terresrrial Sciences Laborarory, Air Force Cambridge Research Laboratories.

Mechanics of Faulting and Thrust Sheets

Angelier, J. 1984. Tectonic analysis of fault slip data sets. *J. Geophys. Res.* 89(B7): 5835–5848.

Hafner, W. 1951. Stress distributions and faulting. *Geol. Soc. Am. Bull.* 62: 373–398.

Hubbert, M. K., and W. W. Rubey. 1959. Role of fluid pressure in mechanics of overthrust faulting. *Geol. Soc. Am. Bull.* 70: 115–206.

Chapple, W. M. 1978. Mechanics of thin-skinned fold-and-thrust belts. *Geol. Soc. Am. Bull.* 25: 1189–1198.

Dahlen, F. A., J. Suppe, and D. Davis. 1984. Mechanics of fold-and-thrust belts and accretionary wedges: Cohesive Coulomb theory. *J. Geophys. Research* 89: 10,087–10,101.

Dahlen, F. A. 1984. Noncohesive critical coulomb wedges: An exacr solution. *J. Geophys. Research* 89: 10,125–10,133.

Davis, D., J. Suppe, and F. A. Dahlen. 1983. Mechanics of fold-and-thrust belts and accrerionary wedges. *J. Geophys. Research* 88: 1153–1172.

Davis, D., and T. Engelder. 1985. The role of rock salt in fold-and-thrust belts. *Tectonophysics* 119: 67–88.

Elliot, D. 1976. The motion of thrust sheets. *J. Geophys. Research* 81: 949–963.

Emerman, S., and D. Turcotte. 1983. A fluid model for the shape of accretionary wedges. *Earth and Planet. Sci. Letts.* 63: 379–384.

Scholz, C. H. 1990. *The mechanics of earthquakes and faulting.* New York: Cambridge University Press.

Stockmal, G. S. 1983. Modeling of large-scale accretionary wedge formation. *J. Geophys. Research* 88: 8271–8287.

Twiss, R. J., G. M. Protzman, and S. D. Hurst. 1991. Theory of slickenline parterns based on the velocity gradient rensor and microroration. *Tectonophysics* 186: 215–239.